Enhancing Selectivity through Forced Dynamic Operation with Intraparticle Diffusion Limitations: Ethane Oxidative Dehydrogenation

Austin Morales, Praveen Bollini[+] and Michael Harold[+]

William A. Brookshire Department of Chemical and Biomolecular Engineering

Houston, TX 77204-4004

[+]Corresponding Authors: ppbollini@uh.edu; mharold@uh.edu

Abstract

During steady state operation (SSO) of industrial fixed-bed reactors, typically containing millimeter-sized or larger pellets to limit pressure drop, diffusion limitations are unavoidable. Well-known impacts of diffusion limitations include the reduced rate of a positive order reaction and reduced selectivity of the desired intermediate product in a sequential reaction system. This work presents an approach for circumventing diffusion limitations through forced dynamic operation (FDO) of metal oxide catalyzed partial oxidation reactions. Through coupled experiments and modeling, we examine the use of FDO to mitigate selectivity losses of the intermediate product in a parallel-consecutive reaction. With the oxidative dehydrogenation (ODH) of ethane (C_2H_6) to ethylene (C_2H_4) over an Al_2O_3 supported VO_x catalyst as the model reaction system, FDO is shown to mitigate undesired C_2H_4 overoxidation to CO_x that predominates in steady state diffusion-limited pellets, resulting in C_2H_4 selectivities that are 15% (absolute) higher compared to SSO in 2.6 mm catalyst pellets. A kinetic model reveals that FDO beneficially alters the distribution of chemisorbed (O_*) and lattice (O_L) oxygen, which respectively primarily participate in reactions consuming C_2H_4 and C_2H_6. During SSO the detrimental impact of diffusion limitations on the intermediate selectivity and sustained refilling of O_* from bulk phase O_2 results in a decrease in C_2H_4 selectivity with increasing ethane conversion. During FDO, C_2H_4 generated within the pellet reacts with unselective O_*, leaving behind selective O_L. The reduced bulk phase O_2 in the reductive half cycle leads to an accumulation of O_L, which suppresses C_2H_4 overoxidation to CO_x. This effect is amplified via C_2H_4 trapping in the catalyst pellet. Thus, larger catalyst pellets exhibit selectivities that more rapidly increase with reduction time, thereby inducing higher FDO cycle averages compared to SSO. The findings raise the prospect of applying FDO through feed switching or chemical looping as a way to increase intermediate yield in the class of partial oxidation reactions.

Keywords: Ethane; Ethylene; Selective Oxidation; Forced Dynamic Operation; Diffusion; Oxidative Dehydrogenation

1. Introduction

Oxidative dehydrogenation (ODH) of ethane (C_2H_6) to ethylene (C_2H_4) has long been touted as a promising alternative to conventional ethane steam cracking [1-6]. In contrast to the endothermic cracking, exothermic ODH does not require extensive combustion for heating and in fact can be operated autothermally [1-6]. On the other hand, ODH typically has lower ethylene yields due primarily to CO and CO_2 formation. For instance, ODH has demonstrated ethylene yields as high as 46% at 20% ethane conversion whereas conventional steam cracking achieves yields as high as 50% at 70% conversion [1]. In addition, undesired oxygenates such as acetic acid may be formed, complicating downstream separations. A large number of mechanistic studies have been conducted to elucidate the kinetics of ethane ODH over various catalysts [3][5-9].

Reactor design and scale up considerations for ODH require a detailed understanding of the coupling between the catalytic kinetics and transport processes [4][10-16]. A table listing industrial reactors and catalysts is included in S1 of the supplemental information (SI). Previous studies have explored alternative reactor operation and design issues for ethane ODH including autothermal operation, chemical looping, and membrane reactors [16-26]. As shown in several works, overoxidation of the desired intermediate product, C_2H_4 to CO_x in the ethane ODH reaction system, is strongly affected by intraparticle (intrapellet, pore) diffusion [10-16][27]. It is well established that intraparticle diffusion in sequential reaction networks can reduce the yield of intermediates, which are typically the desired products [10-16][27]. As a result, there have been attempts to reduce selectivity losses caused by intrapellet diffusion limitations [10-14][15]. In this study, we demonstrate the use of FDO to reduce ethylene overoxidation rates in diffusion-controlled catalysts during ethane ODH.

Previous studies have shown that catalytic selective oxidation may involve the participation of more than one type of oxygen species [15][17][20][23-25][28-31]. The two types frequently proposed are chemisorbed oxygen (O_*) and lattice oxygen (O_L) [17][20][28-29]. Oxygen bound to the surface is referred to as chemisorbed oxygen and is speculated to be electrophilic [17][20][28-29]. The electrophilicity of chemisorbed oxygen suggests that it is inclined to sever the electron dense C-C and C=C bonds forming CO_x. The oxygen stored within the metal oxide is referred to as lattice oxygen and is considered nucleophilic [17][20][28-29]. The nucleophilicity of the lattice oxygen suggests that it instead preserves C-C bonds and therefore only abstracts hydrogen subsequentially forming ethylene [17][20][28-29]. There have been numerous attempts to experimentally discern between chemisorbed and lattice oxygen species through techniques such as Raman and TAP reactor analysis [33-35]. These methods suggest chemisorbed and lattice oxygen are located on the surface and within the metal oxide crystallite, respectively, hence their electrophilic and nucleophilic properties [9][29][33-35].

Reactivity differences between chemisorbed and lattice oxygen has inspired the development of alternative reactor designs and operating schemes centered around promoting reactions between ethane and selective lattice oxygen [15][17][20][23-25][28-31]. One such mode being forced dynamic operation (FDO) of chemical reactors has been demonstrated as a viable means of improving selectivities of total and selective oxidation reactions including, but not limited to, ethane ODH, butane to maleic anhydride, propane ODH, propene ammoxidation, ethylene epoxidation and others [15][17][24][29][36-38]. A challenge associated with FDO involves the search for a catalyst that is capable of outperforming conventional steady state operation (SSO). It has been shown that ethylene selectivity enhancement achieved in membrane and dynamically-operated reactors are linked to apparent reaction orders of selective and

unselective reactions [32][23][27]. Specifically, higher selectivities are achievable when the apparent reaction order of the modulated species in a dynamic reactor and permeate in a membrane reactor is higher for the unselective relative to the selective rate [3][32][23][27]. For instance, Skoufa *et. al.* increased ethylene selectivities by 3% via a distributed oxygen feed during ethane ODH over a NiNbO catalyst where selective and unselective reactions had apparent oxygen orders of 0.21 and 0.83/ 0.32 respectively [3]. Others such as Waku *et. al.* found no difference between membrane and co-feed selectivities for the same chemistry over a VO_x Al_2O_3 catalyst which they attributed to all reactions having the same dependency (0^{th} order) on oxygen concentrations [23]. Only upon the introduction of oxygen dependent homogenous gaseous reactions (at elevated temperatures) did membrane reactors yield higher selectivities than their co-feed counterparts [23]. Our previous work was able to increase the ethylene selectivity by as much as 10% through FDO when the difference between unselective and selective apparent oxygen orders was 0.4 over an MoO_x Al_2O_3 catalyst which had selective and unselective reaction orders of 0 and 0.3 [32]. Like Waku *et. al.*, our work found FDO selectivities over VO_x catalysts to be similar to those achieved during SSO due to all rates being 0^{th} order in oxygen. While the aforementioned studies thoroughly investigated selectivity enhancement through kinetics, they do not encroach on other relevant reactor phenomena such as intrapellet diffusion. This publication will explore an alternative mode of FDO enhancement by exploiting diffusion limitations within catalyst pellets, rather than kinetics alone, to improve ethylene selectivities.

In this study, through a combination of targeted experiments and modeling, we explore the use of FDO to mitigate selectivity losses and improve ethylene selectivities in diffusion-controlled catalyst pellets. We show that higher selectivities are achievable through FDO in the presence of intrapellet diffusion, despite selective and unselective reactions having the same apparent reaction

orders. FDO is shown to reduce C_2H_4 selectivity losses caused by intrapellet diffusion during steady state operation (SSO) of C_2H_6 ODH over VO_x Al_2O_3 catalysts. The enhanced ethylene selectivity is achieved through a favored reduction of unselective chemisorbed oxygen in the absence of gas phase oxygen, leading to an accumulation of selective lattice oxygen. The findings suggest that a larger unselective (than selective) oxygen reaction order is not a requirement for selectivity enhancement via FDO. Thus, intrapellet diffusion can be leveraged to achieve a dynamic enhancement despite the lack of oxygen pressure dependencies (0^{th} order) in the reaction network.

2. Experimental Methods

The VO_x (3wt%) on γ-Al_2O_3 catalyst pellets were synthesized through incipient wetness impregnation. Oxalic acid (Sigma Aldrich) was added to a solution of 0.15 M ammonium metavanadate (Sigma Aldrich) in 10 mL of deionized (DI) water until the pH reached 2, ensuring complete dissolution of precursor [5][7][39]. The resulting ammonium metavanadate and oxalic acid solution was pipetted dropwise onto 4.85 g of γ-Al_2O_3 powder (Sigma Aldrich). The resulting paste was dried overnight at 120 °C. The sample was subsequently calcined at 600 °C for 6 hours in air (99.99% Praxair) flowing at 0.5 L/min [5][7]. The resulting solid was pelletized at 3000 psi for 1min, then crushed and sieved to create particles in the following sizes: 0.180-0.425, 0.8-1.0, 1.7-2.0 and 2.4-2.8 mm. The average size in each range will be used to refer to the corresponding samples; i.e., 0.3, 0.9, 1.85 and 2.6 mm. >1 mm pellets were investigated in this study due to their relevance in industrial sized reactors; as smaller, <1 mm pellets are typically unused due to excessive pressure drop generated across the bed. Thus, larger pellets would allow for the investigation of both kinetic and transport effects on FDO performance.

Flow reactor studies were conducted in a 4 mm ID quartz tube reactor, with temperature control achieved using a tube furnace. Temperatures were measured with two thermocouples positioned 3 mm from the inlet and outlet of the catalyst bed. The catalysts were pretreated in 10% O_2 in N_2 at 600°C for 30 minutes before each experiment. Feed concentration forcing was achieved by managing two streams [3% C_2H_6 in N_2 (UHP; Praxair) + O_2 (10% in N_2 (UHP; Praxair) or 100%)], with two, 4-way actuator values from VICI Valco (see schematic S1 in SI). Each valve switches between reactants (C_2H_6 and O_2) at a prescribed frequency and a separate nitrogen feed to maintain a constant overall flow rate. FDO experiments were conducted with reactants pulsed within 2-minute periods and a 50% duty cycle (1 min on, 1 min off). A schematic of the reactor set up and examples of reactant concentration profiles versus time are provided in S2 and S3, respectively. To remain outside of the flammability regime, hydrocarbon rich and lean feeds were considered. In hydrocarbon rich cases, the concentrations of C_2H_6 and O_2 can be as high as 50 and 10% respectively to remain outside of the flammability zone [4]. In hydrocarbon lean conditions, concentrations may fall around 3% with oxygen concentrations of 15% [29]. Since this study utilized a metal oxide catalyst, rich C_2H_6 conditions would rapidly reduce the catalyst in the absence of O_2 during the reduction half cycle, thereby requiring higher oscillation frequencies (to prevent irreversible catalyst reduction) than are allowable via our experimental set up. Thus, this study utilizes lean C_2H_6 conditions of 1% cycle average (and 10% cycle average O_2) to remain outside of the flammability zone and prevent overreduction of the metal oxide catalyst. Simultaneously, lean ethane conditions minimize the contributions of heat effects induced by the exothermic reactions thereby focusing this study on the interplay between kinetics and mass transport. The bypass or reactor effluent concentrations of O_2, C_2H_6, and CO_2 were measured using a quadrupole mass spectrometer (Hiden Analytical HPR20) at 32, 30 and 44 m/z respectively. C_2H_4

and CO concentrations were recorded using a Fourier transform infrared (FTIR) spectrometer gas analyzer (MKS). Concentrations were obtained from via a calibration between the concentration and signal intensities of the MS and FTIR. Carbon selectivity and C_2H_6 conversion were respectively determined using eqns. (1) and (2):

$$S_i = \frac{\nu_i \, N_i}{\left(2 \, N_{C_2H_4} + N_{CO} + N_{CO_2}\right)} \tag{1}$$

$$X_{C_2H_6} = \frac{2 \, N_{C_2H_4} + N_{CO} + N_{CO_2}}{2 \, N^f_{C_2H_6}} \tag{2}$$

N_i represents the moles of species i and ν_i represents the number of carbon atoms in species i. During FDO, N_i is the cyclic average moles of species i. Carbon selectivity as a function of ethane conversion was determined by varying catalyst weight and total flow rate such that W/F values varied between 0.5 and 3 mg/sccm. Blank tube tests indicated the absence of homogeneous reactions below 600°C. Presented data had carbon balances of 100±5%. Further information on catalyst characterization such as N_2 physisorption, powder X-ray diffraction (XRD), scanning electron microscopy (SEM), X-ray photoelectron spectroscopy (XPS) and CO TPR can be found in S4-S8.

3. Results and Discussion

3.1. C_2H_6 ODH on VO_x Al_2O_3: Steady State Analytical Solution Considering Intrapellet Diffusion

Supported vanadia catalysts have been shown to be a viable class of materials for ethane and propane ODH due to their high activity [5][7-8][15][30][39-46]. In excess O_2, ethane ODH on the VO_x comprises a network of three first-order reactions in the triangular network, depicted in Scheme 1. Global kinetic parameters (apparent reaction orders and rate constants) were obtained by fitting data to the 0.3mm catalyst pellet which was previously confirmed to be absent of heat

and mass transport limitations [32]. These global kinetic parameters will be used in the following analytical solution presented in this study across all pellet sizes.

To better understand the contribution of intrapellet diffusion on reactor performance we present an analytical solution for SSO of a fixed-bed reactor containing spherical catalytic pellets. Pore diffusion and reaction at an arbitrary point within the reactor is described by [10-14][38]:

$$0 = \left(\frac{1}{\xi^2}\left(\frac{\partial}{\partial \xi}\xi^2 \frac{\partial \boldsymbol{u}}{\partial \xi}\right) - \bar{\bar{\boldsymbol{\phi}}}\,\boldsymbol{u}\right) \tag{3}$$

Eqn. (3) is solved in tandem with the SS bulk phase species plug flow reactor (PFR) balances to quantify the role of intrapellet diffusion on reactor performance. Dimensionless concentrations (u_i) are normalized by the bulk reactor feed concentration of C_2H_6

$$\boldsymbol{u} = \begin{bmatrix} u_{C_2H_6} \\ u_{C_2H_4} \end{bmatrix} = \frac{1}{C^f_{b,C_2H_6}} \begin{bmatrix} C_{C_2H_6} \\ C_{C_2H_4} \end{bmatrix} \tag{4}$$

The Thiele matrix $\bar{\bar{\boldsymbol{\phi}}}$ is given by [10-14]:

$$\bar{\bar{\boldsymbol{\phi}}} = \begin{bmatrix} \phi^2_{C_2H_6,1} + \phi^2_{C_2H_6,2} & 0 \\ -\phi^2_{C_2H_4,1} & \phi^2_{C_2H_4,3} \end{bmatrix} = \begin{bmatrix} \dfrac{k_1 r_p^2}{D_{e,C_2H_6}} + \dfrac{k_2 r_p^2}{D_{e,C_2H_6}} & 0 \\ -\dfrac{k_1 r_p^2}{D_{e,C_2H_4}} & \dfrac{k_3 r_p^2}{D_{e,C_2H_4}} \end{bmatrix} \tag{5}$$

The dimensionless boundary conditions (BC's) at the catalyst pellet center ($\xi = 0$) and edge (radius) ($\xi = 1$) are given as follows:

Pellet center $\xi = 0$:

$$\left(\frac{\partial \boldsymbol{u}}{\partial \xi}\right)_{\xi=0} = \boldsymbol{0} \tag{6}$$

Pellet surface $\xi = 1$:

$$\left(\frac{\partial \boldsymbol{u}}{\partial \xi}\right)_{\xi=1} = \begin{bmatrix} Sh_1 & 0 \\ 0 & Sh_2 \end{bmatrix} \begin{bmatrix} u_{b,C_2H_6} - u_{C_2H_6} \\ u_{b,C_2H_4} - u_{C_2H_4} \end{bmatrix} |_{\xi=1} = \begin{bmatrix} \dfrac{k_{g,C_2H_6} r_p}{D_{e,C_2H_6}} & 0 \\ 0 & \dfrac{k_{g,C_2H_4} r_p}{D_{e,C_2H_4}} \end{bmatrix} \begin{bmatrix} u_{b,C_2H_6} - u_{C_2H_6} \\ u_{b,C_2H_4} - u_{C_2H_4} \end{bmatrix} |_{\xi=1} \tag{7}$$

It has been shown by many that ethane ODH over VOx catalysts is 1st and 0th order in bulk phase (gaseous) C_2H_6 and O_2, respectively [5][7][39]. Experimental validation of these orders is confirmed in the current study in later sections. Assuming that O_2 is in stoichiometric excess and is assumed constant, the resulting system of material balances is linear and has a closed-form solution. The solution is solved by uncoupling the species balances (diagonalizing) with eigen values and vectors [45-47]. A complete derivation of the SS solution is presented in S9. The dimensionless solutions of C_2H_6 and C_2H_4 within a spherical catalyst pellet are given by the following equation:

$$u_{C_2H_6} = \frac{u_{b,C_2H_6}}{\xi} \frac{Sh_1 \tanh(\xi\, \phi_{12})}{\sqrt{\phi_{C_2H_6,1}^2 + \phi_{C_2H_6,2}^2} + (Sh_1 - 1)\tanh(\phi_{12})} \tag{8}$$

Assuming $Sh_{C_2H_6} \approx Sh_{C_2H_4}$ (given the similarity between C_2H_6 and C_2H_4), the dimensionless concentration of C_2H_4 is given by:

$$u_{C_2H_4} = \frac{u_{b,C_2H_6}}{\xi} \frac{\beta\, Sh_1 \tanh\left(\xi \sqrt{\phi_{C_2H_6,1}^2 + \phi_{C_2H_6,2}^2}\right)}{\sqrt{\phi_{C_2H_6,1}^2 + \phi_{C_2H_6,2}^2} + (Sh_1 - 1)\tanh\left(\sqrt{\phi_{C_2H_6,1}^2 + \phi_{C_2H_6,2}^2}\right)} + \frac{u_{b,C_2H_4} - \beta\, u_{b,C_2H_6}}{\xi} \frac{Sh_2 \tanh\left(\xi\, \phi_{C_2H_4,3}\right)}{\phi_{C_2H_4,3} + (Sh_2 - 1)\tanh\left(\phi_{C_2H_4,3}\right)} \tag{9}$$

With the following parameter defined:

$$\beta = \frac{\phi_{C_2H_4,1}^2}{\left(\phi_{C_2H_4,3}^2 - \phi_{C_2H_6,1}^2 + \phi_{C_2H_6,2}^2\right)} = \frac{k_1}{k_3 - \frac{D_{e,C_2H_4}}{D_{e,C_2H_6}}(k_1 + k_2)} \tag{10}$$

the effectiveness factors for reactions 1-3 in Scheme 1 are given by [10-11][13-14]

$$\eta_1 = \eta_2 = \frac{3\ Sh_1 \left(\sqrt{\phi_{C_2H_6,1}^2 + \phi_{C_2H_6,2}^2} - \tanh\left(\sqrt{\phi_{C_2H_6,1}^2 + \phi_{C_2H_6,2}^2}\right)\right)}{\left(\phi_{C_2H_6,1}^2 + \phi_{C_2H_6,2}^2\right)\left(\sqrt{\phi_{C_2H_6,1}^2 + \phi_{C_2H_6,2}^2} + (Sh_1 - 1)\tanh\left(\sqrt{\phi_{C_2H_6,1}^2 + \phi_{C_2H_6,2}^2}\right)\right)} \tag{11}$$

$$\eta_3 = \beta\left(\frac{u_{b,C_2H_6}}{u_{b,C_2H_4}}\right)\left(\eta_1 - \eta'_3\right) + \eta'_3 \tag{12}$$

where η'_3 is the effectiveness factor for reaction 3 in the uncoupled problem:

$$\eta'_3 = \frac{3\,Sh_2\left(\phi_{C_2H_4,3} - \tanh\left(\phi_{C_2H_4,3}\right)\right)}{\phi^2_{C_2H_4,3}\left(\phi_{C_2H_4,3} + (Sh_2 - 1)\tanh\left(\phi_{C_2H_4,3}\right)\right)} \tag{13}$$

Note that η_3 is a function of bulk phase concentrations due to the coupling between C_2H_6 and C_2H_4 balances. η_3 is affected by C_2H_4 produced via C_2H_6 within the catalyst pellet through ODH. This coupling is discussed in later sections.

With effectiveness factors determined, one can now evaluate the axial concentration profiles through the following SS design equation accounting for convection and reaction:

$$0 = \left(-\frac{\partial \boldsymbol{u_b}}{\partial \gamma} - \overline{\overline{\boldsymbol{Da}}}\,\boldsymbol{u_b}\right) \tag{14}$$

where γ is the dimensionless reactor length and $\overline{\overline{\boldsymbol{Da}}}$ is the Damköhler number matrix defined as

$$\overline{\overline{\boldsymbol{Da}}} = \begin{bmatrix} \eta_1(Da_1 + Da_2) & 0 \\ -\eta_1\,Da_1 & \eta_3\,Da_3 \end{bmatrix} = \tau \begin{bmatrix} \eta_1(k_1 + k_2) & 0 \\ -\eta_1\,k_1 & \eta_3\,k_3 \end{bmatrix} \tag{15}$$

For a pure feed of C_2H_6, the following boundary condition applies:

$$\boldsymbol{u_b}(\gamma = 0) = \begin{bmatrix} u_{b,C_2H_6} \\ u_{b,C_2H_4} \end{bmatrix} = \begin{bmatrix} 1 \\ 0 \end{bmatrix} \tag{16}$$

Evaluating eqns. (15) and (16) results in the following dimensionless bulk phase C_2H_6, C_2H_4 and CO_x profiles as a function of γ (see S9 for details):

$$u_{b,C_2H_6} = \exp(-(Da_1 + Da_2)\eta_1\gamma) \tag{17}$$

$$u_{b,C_2H_4} = \frac{a_2}{a_1 - 1}\left(\exp\left(-Da_3\eta'_3\gamma\right) - \exp(-(Da_1 + Da_2)\eta_1\gamma)\right) \tag{18}$$

$$u_{b,CO_x} = 2 * \left(1 - \exp(-(Da_1 + Da_2)\eta_1\gamma) - \frac{a_2}{a_1 - 1}\left(\exp\left(-Da_3\eta'_3\gamma\right) - \exp(-(Da_1 + Da_2)\eta_1\gamma)\right)\right) \tag{19}$$

where the constants a_1 and a_2 are the following:

$$a_1 = \frac{\eta'_3 \, Da_3}{\eta_1(Da_1 + Da_2)} \; and \; a_2 = \frac{\left(Da_3 \, \beta\left(\eta_1 - \eta'_3\right) - \eta_1 Da_1\right)}{\eta_1(Da_1 + Da_2)} \tag{20}$$

It is noted that in the limit of no mass transfer limitations ($\eta_1 = \eta_2 = \eta_3 = 1$), eqn. (18) collapses into the solution derived by Khodakov *et. al.* for propane ODH having the same kinetics without diffusion limitations (see S10) [40]. Predictions from the SS analytical solutions are compared to experimental results in later sections. The following section provides a comparison between experimental results and solutions above to demonstrate how intrapellet diffusion affects the paths to CO_x formation.

3.2. Effect of intrapellet diffusion on rates and apparent activation energies

It is known that intrapellet diffusion can alter the observed reaction orders and activation energies [10-14]. We exploit this fact to determine the presence of intrapellet diffusion limitations by comparing model-predicted and experimentally measured apparent activation energies as a function of the pellet radius. Table 1 lists apparent activation energies of C_2H_4 and CO_x formation rates for all catalyst pellet sizes, measured experimentally and estimated by the analytical solution. Experimental apparent activation energies were measured under differential conditions (< 10% conversion of the limiting reactant, C_2H_6) by quantifying the slopes of ln(r) versus 1/RT plots (provided in S11). Model-estimated apparent activation energies were obtained by simulating the aforementioned experiments using rate constants obtained from previous works [5][32]. The intrinsic activation energy for reaction 3 in Scheme 1 was determined from work by Argyle *et. al.* which found the difference between activation energies of ODH and C_2H_4 combustion to be approximately 45 kJ mol^{-1} for this VO_x weight loading [7]. This relationship was applied to this work to determine the activation energy of C_2H_4 combustion. Experimentally measured activation energies for the smallest pellet size (0.3mm) are 90.9, 104 and 107 kJ mol^{-1} for C_2H_4 and CO + CO_2 formation from C_2H_6, respectively. These values are similar to those found by Argyle *et. al.*

who reported activation energies of 120 and 100 kJ mol^{-1} for C_2H_6 ODH and combustion, respectively [5]. Others such as Le Bars *et. al.* reported activation energies of 97 and 101 kJ mol^{-1} for C_2H_6 ODH and combustion, respectively [43].

Table 1: Apparent activation energies for C_2H_4 and CO_x formation rates measured experimentally and estimated by the analytical solution, eqns. (17-19) for various pellet sizes.

	Experiment			**Analytical Solution**	
Catalyst Size [mm]	$E_{a,C_2H_4}^{app}$ **[kJ/mol]**	$E_{a,CO}^{app}$ **[kJ/mol]**	E_{a,CO_2}^{app} **[kJ/mol]**	$E_{a,C_2H_4}^{app}$ **[kJ/mol]**	E_{a,CO_x}^{app} **[kJ/mol]**
0.18-0.425	90.9	104	107	83.8	101
0.8-1.0	73.9	100	93.0	73.4	99.3
1.7-2.0	56.8	94.6	87.7	59.6	88.5
2.4-2.8	51.9	76.6	87.0	56.4	82.7

Overall, good agreement is obtained between the measurements and model predictions. Table 1 shows that the experimentally measured apparent activation energy of C_2H_4 formation decreases from 90.9 to 51.9 kJ mol^{-1} with the pellet size increasing from 0.3 to 2.6mm. Table 1 also shows that the analytical solution predicts a decrease in the apparent activation energy from 83.8 to 56.4 kJ mol^{-1} with increasing intrapellet diffusion limitations (pellet size). The decrease is an expected result: A single first-order catalytic reaction has an apparent activation energy under strong diffusion limitations that is one-half the intrinsic value [10-14]. The textbook 50% decrease in the 0.3mm catalyst pellet apparent activation energy with pellet diameter suggests the measured 90.9 kJ mol^{-1} is indeed near the intrinsic value. On the other hand, Table 1 shows that the

experimental apparent activation energies for CO and CO_2 formation only decrease by 25% (104 &107 kJ/mole to 77 & 87 kJ/mole) rather than 50%. This might suggest a deviation from the expected result. However, this has to do with features of the multi-reaction network not present for the single reaction system. That is, the overall rate constant for CO_x formation is less sensitive to catalyst pellet size than that of C_2H_4 formation. The measured decrease in the apparent activation energy for CO and CO_2 formation is validated by the apparent activation energy decrease for CO_x predicted by the analytical solution (101 to 82.7 kJ/mole). Subsequent paragraphs discuss a more rigorous analysis of the analytical solution and its implications on the effects of intrapellet diffusion on activation energy.

The consistency between experiment and theory warrants a more detailed investigation into the effects of intrapellet diffusion on the apparent activation energy of CO_x formation. Consider the overall rates of formation of C_2H_4 and CO_x derived in section 3.1:

$$r_{C_2H_4} = \eta_1 k_1 u_{b,C_2H_6} - \eta_3 k_3 u_{b,C_2H_4} = \left(\eta_1 k_1 - k_3\left[\beta(\eta_1 - \eta_3') + \eta_3' \frac{u_{b,C_2H_4}}{u_{b,C_2H_6}}\right]\right) u_{b,C_2H_6}$$
$$= k_{ov,C_2H_4} u_{b,C_2H_6} \quad (21)$$

$$r_{CO_x} = \eta_1 k_2 u_{b,C_2H_6} + \eta_3 k_3 u_{b,C_2H_4} = \left(\eta_1 k_2 + k_3\left[\beta(\eta_1 - \eta_3') + \eta_3' \frac{u_{b,C_2H_4}}{u_{b,C_2H_6}}\right]\right) u_{b,C_2H_6}$$
$$= k_{ov,CO_x} u_{b,C_2H_6} \quad (22)$$

The apparent activation energies for C_2H_4 and CO_x formations ($E_{a,C_2H_4}^{app}$ and E_{a,CO_x}^{app}) can be determined from the overall rate constants (k_{ov,C_2H_4} and k_{ov,CO_x}) measured under differential conditions, given by eqns. (21) and (22), respectively. Here we consider how the definitions of overall rate constants influence the measured apparent activation energies for two cases: kinetic control and diffusion control. At low conversions $\left(\frac{u_{b,C_2H_4}}{u_{b,C_2H_6}} \approx 0\right)$ and under kinetic control (no mass transfer limitations; $\eta_1 \approx \eta_2 \approx \eta'_3 \approx 1$), it can be shown that $k_{ov,C_2H_4} \approx k_1$ and $k_{ov,CO_x} \approx k_2$.

This is an expected result in the absence of diffusion limitations at low C_2H_6 conversions (see S12 for details). When intrapellet diffusion limitations are not negligible (i.e., $\eta_1 < 1$ and $\eta'_3 < 1$), the overall rate constants for C_2H_4 and CO_x are given by the entire expression in eqns. (21) and (22), respectively. A comparison of the relative magnitudes of the first ($\eta_1 k_1$) and second $\left(k_3\left[\beta(\eta_1 - \eta'_3) + \eta'_3 \frac{u_{b,C_2H_4}}{u_{b,C_2H_6}}\right]\right)$ terms is necessary. We define the effective rate constants for reactions 1-3 in scheme 1 as follows:

$$k_{eff,1} = \eta_1 k_1 \tag{23}$$

$$k_{eff,2} = \eta_2 k_2 \tag{24}$$

$$k_{eff,3} = k_3\left[\beta(\eta_1 - \eta'_3) + \eta'_3 \frac{u_{b,C_2H_4}}{u_{b,C_2H_6}}\right] \tag{25}$$

Figs. 1A and B plot the effective rate constants from eqns. (23)-(25), along with the C_2H_4 and CO_x overall formation rate constants eqn. (21)-(22) at 500 and 550°C, conditions satisfying the differential assumption. Figs. 1A and B show that for all catalyst pellet sizes and conversions, $k_{eff,1} \gg k_{eff,3}$. Thus, the overall rate constant for C_2H_4 formation may be approximated by:

$$k_{ov,C_2H_4} \approx \eta_1 k_1 \tag{26}$$

Eqn. (26) indicates that, at low conversion, the net formation rate of C_2H_4 is equal to its production by C_2H_6 ODH and is unaffected by C_2H_4 combustion. The apparent activation energy in the presence of strong diffusion limitations therefore becomes similar to the classic single reaction problem shown below (see S12 for detailed derivation) [10-14]:

$$E^{app}_{a,C_2H_4} \approx \frac{E^{int}_{a,C_2H_4}}{2} \tag{27}$$

This solution is consistent with experimental results in Table 1 and the derivation considering a single first order reaction within a catalyst pellet [10-14].

Following suit, we evaluate the relative magnitudes of $k_{eff,2}$ (eqn. (24)) and $k_{eff,3}$ (eqn. (25)) to identify the dominant term in eqn. (22). Previous works including our recent work have shown that $k_2 < k_3$, indicating that the overall rate constant for CO_x formation when $\eta_i << 1$ (strong diffusion control) is approximated by [5][7][32]:

$$k_{ov,CO_x} \approx \left(k_3 \left[\beta(\eta_1 - \eta_3') + \eta_3' \frac{u_{b,C_2H_4}}{u_{b,C_2H_6}} \right] \right) \tag{28}$$

Plotting eqn. (28) in Figs. 1A and B, it is observed that $k_{eff,3}$ slightly increases with increasing pellet size, while $k_{eff,2}$ decreases. Thus, larger catalyst pellets (longer diffusion times) have a higher effective rate constant for C_2H_4 overoxidation to CO_x. This trend agrees with the classical result that diffusion limitations reduce intermediate product yields in a consecutive reaction system [10-14]. The reduction is a result of longer time spent by the ODH intermediate C_2H_4 in the pellet, increasing its likelihood of over oxidizing to CO_x. The result is an increase in the effective C_2H_4 oxidation rate constant with increasing pellet size. The decrease in $k_{eff,2}$ with increasing pellet size is a result of the decreasing effectiveness η_2, recalling $\eta_2 = \eta_1$. That is, the lower $k_{eff,2}$ is simply a result of a decreased utilization of the catalyst pellet by C_2H_6. Fig. 1A shows that $k_{eff,2}$ and $k_{eff,3}$ intersect at a pellet radius of 0.3 mm at 500°C. To the left of this intersection, $k_{eff,2}$ is greater than $k_{eff,3}$ indicating that CO_x production is dominated by C_2H_6 overoxidation; to the right it is dominated by C_2H_4 overoxidation (i.e., $k_{eff,3}$ is greater than $k_{eff,2}$). Intrapellet diffusion time scales control the dominant route of CO_x production (i.e., via C_2H_6 or C_2H_4 overoxidation) in the triangular reaction network. As will be seen in later sections, this effect can be exploited during FDO to change the type of oxygen species consumed during CO_x production.

Since catalyst pellet size has been shown to affect the relative contributions of r_2 and r_3 towards CO_x production, one can better understand the independence of E_{a,CO_x}^{app} with respect to

pellet radii. Figs. 1A and B show that despite the shift in dominant pathways, the overall rate constant for CO_x production (k_{ov,CO_x}) remains nearly independent of pellet radius. Ultimately, $k_{eff,3}$ and $k_{eff,2}$ increase and decrease, respectively, making their sum (k_{eff,CO_x}) nearly independent of catalyst pellet size, hence the similarities in E_{a,CO_x}^{app} over the range of pellet radii presented in Table 1.

In summary, the analytical results suggest that the measured apparent activation energy for C_2H_4 formation is approximately one-half the intrinsic value and CO_x formation is nearly unchanged in the presence of diffusion limitations. These results are indeed observed in experimental results presented in Table 1. Ultimately, the analytical solution and experimental data suggest that as the pellet radius increases, more C_2H_4 will over oxidize to CO_x resulting in lower selectivities. C_2H_4 overoxidation is therefore the primary mode of CO_x production, even at low C_2H_6 conversions of 5-10%.

These trends are captured experimentally in Fig. 2 which plots C_2H_4 and CO_x formation rates at 550°C and 0.5 mg sccm^{-1} for several pellet sizes. The data shows that the C_2H_4 formation rate decreases with pellet size, in agreement with Table 1 and Figs. 1A-B. As described earlier, the C_2H_4 formation rate decreases due to C_2H_6 intrapellet concentration gradients. On the other hand, Fig. 2 shows that the CO_x formation rate increases to a maximum at 0.9 mm followed by a gradual decrease. As discussed above, C_2H_6 and C_2H_4 overoxidation rates decrease and increase, respectively, and the overall CO_x formation rate is less affected by intrapellet diffusion than the ethane consumption rate. The initial increase in the CO_x formation rate from 0.3 to 0.9 mm is due to C_2H_4 overoxidation rates increasing with increasing pellet size due to its trapping within the catalyst pores. This initial increase is also captured but to a lesser degree in Fig. 1B which shows predictions of the analytical solution; the plot shows a slight increase in the overall CO_x formation

rate constant from 107 to 122 min^{-1}. Fig. 2 shows the CO_x formation rate only decreases by 19% (from 68 to 55 μmol min^{-1} g-cat^{-1}) when increasing the pellet size from 0.9 to 2.6 mm whereas the C_2H_4 formation rate decreases by 61% (from 68 to 26 μmol min^{-1} g-cat^{-1}). In comparison, Fig. 1B shows that the overall CO_x and C_2H_4 rate constants decrease by 12% (from 146 to 128 min^{-1}) and 52% (from 152 to 74 min^{-1}) respectively. These results indicate that the C_2H_4 formation rate decreases more rapidly with pellet size than the CO_x formation rate due to slower intrapellet diffusion rates, resulting in lower C_2H_4 selectivity at the reactor scale. The following section will demonstrate how these C_2H_4 selectivity losses can be mitigated through FDO.

3.3: Mass transfer assisted dynamic operation of ethane ODH: Experimental results

In the previous section we show that diffusion limitations can shift the dominant CO_x production pathway from C_2H_6 to C_2H_4 oxidation. This section investigates the effect of diffusion limitations for the various VO_x catalyst sizes during FDO. Pellet sizes were selected such that overall rates ranged from kinetic control (0.3mm) to diffusion control (2.6mm). FDO consists of an out-of-phase oscillating feed of C_2H_6 and O_2 with a 50% duty cycle and 2min period (1min on, 1min off). It is noted that the rates of each of the three reactions in Scheme 1 are reduced in the absence of gaseous O_2. As a result, longer residence times are needed during FDO to achieve the same ethane conversion as during SSO. The C_2H_4 selectivities obtained during FDO and SSO are therefore compared at the same C_2H_6 conversion [23][32]. Figs. 3A-D plot C_2H_4 carbon selectivities as functions of C_2H_6 conversion for 0.3, 0.9, 1.85, and 2.6mm catalyst pellets measured experimentally, estimated by a numerical model (to be discussed in later sections) and predicted by the analytical solution derived in section 3.1. Selectivity versus conversion plots containing all products and their respective error bar estimations are provided in S13.

Fig. 3A shows that the kinetically controlled 0.3 mm catalyst pellets, as expected, exhibit no selectivity differences between FDO and SSO. In our earlier experimental study of ethane ODH, we showed that comparable FDO and SSO selectivities versus conversion are a result of all rates over the VO_x catalyst being independent of gas phase O_2 concentration (0^{th} order in O_2) [32]. This result is consistent with Waku *et. al.* who reported a similar finding for co-feed and distributed feed operation of ethane ODH over the same catalyst [23]. Fig. 4 plots the C_2H_4 and CO_x selectivities and C_2H_6 consumption rates as a function of O_2 concentration for kinetically controlled (0.3 mm; Fig. 4A) and diffusion controlled (2.6 mm; Fig. 4B) pellets. Fig. 4A indeed shows that C_2H_6 consumption rates and product selectivities are independent of O_2 concentration. This is the basis for the equivalent selectivities obtained during FDO and SSO in Fig 3A [32].

On the other hand, Figs. 3A-D shows that the difference between FDO and SSO selectivities increases with catalyst pellet size, an unexpected result. While both decrease with increasing pellet size, the SSO selectivity decreases faster than the FDO selectivity. As discussed above, decreasing selectivities are a result of longer diffusion path lengths which increase the extent of C_2H_4 overoxidation to CO_x. Also shown in Figs. 3A-D are the model predictions. The SSO experiments were simulated using both analytical and numerical models, indicated by the dashed and solid lines, respectively. The value was validated through implementation in the 0.3, 0.9 and 1.8mm analytical solutions and all (0.3-2.6mm) numerical evaluations potted in Figs. 3A-D. Excellent agreement between model and experiment is evident. The SSO model confirms that the C_2H_4 selectivity decreases with increasing catalyst pellet size. Later on we investigate the effect of pellet size during FDO using a transient reactor model with more detailed kinetics.

It is known that under diffusion control, the apparent reaction order for the limiting reactant is given by $\left(n_{app} = \frac{n_{int}+1}{2}\right)$ [10-14]. It is reasonable to consider that differences in selectivity

versus conversion trends observed in Figs. 3A-D to be a result of different apparent reaction orders induced by the diffusion limitations. To examine this point, we investigated the impact of diffusion on reaction through rate and selectivity dependencies on O_2 concentration. Figs. 4A and B show that the consumption rates of C_2H_6 over two different sized catalysts are independent of O_2 concentration. This indicates that the primary reactions (involving C_2H_6) are 0^{th} order in O_2 for both catalysts within the concentration range considered. Furthermore, Figs. 4A and B show for each particle size that C_2H_4 and CO_x selectivities are independent of O_2 concentration. The independence of C_2H_6 consumption and product selectivities on O_2 concentration confirm that all the rates in Scheme 1 are indeed 0^{th} order in O_2, for both sized catalysts. The result for kinetically controlled catalysts is further confirmed by several other works in the literature [5][7-8][23]. Thus, differences in selectivity versus conversion trends evident in Figs. 3A-D are not a result of changes in the apparent kinetics due to diffusion limitations. Finally, it has been shown that diffusion limitations primarily affect the kinetics of the limiting reactant which in this case is C_2H_6. Since C_2H_6 is the limiting reactant and is 1^{st} order, its apparent order over all rates will remain unchanged in the presence of strong diffusion control [10-14]. It is further noted that during FDO, C_2H_4 selectivities continue to decrease with increasing catalyst pellet size (Figs. 3A-D). However, the selectivity decrease for FDO is not as significant as that observed during SSO. Thus, FDO merely reduces C_2H_4 selectivity losses due to intrapellet diffusion but does not eliminate them.

3.4: Mass transfer assisted dynamic operation of ethane ODH: Reactor modeling

The previous section demonstrated that higher C_2H_4 selectivities versus C_2H_6 conversion are achieved through FDO of diffusion-controlled catalyst pellets. The SS model lacks essential features that only a transient model can provide, such as the accumulation and consumption of multiple oxygen species throughout the FDO cycle. In this section we describe a transient reactor

model with detailed kinetics, used to pinpoint the underlying cause for the higher C_2H_4 selectivity during FDO relative to SSO.

Our previous work presented the development of the transient kinetic model for ethane ODH [32]. Here we highlight the key features of an updated model in Scheme 2, which successfully predicts the features of FDO and SSO to even higher residence times than those presented in previous works [32]. Scheme 2 proposes that C_2H_6 consumption utilizes lattice oxygen whereas ethylene consumption utilizes lattice and chemisorbed oxygen. The scheme is consistent with previous works assigning electrophilicity and nucleophilicity to chemisorbed and lattice oxygen, respectively [17][20][28-29]. The electrophilicity of chemisorbed oxygen promotes cleavage of electron-dense C=C bonds, forming CO_x. Conversely, nucleophilic lattice oxygen promotes hydrogen abstraction, preserving the C-C bond and forming C_2H_4. On the other hand, the data suggest that C_2H_6 overoxidation involves lattice oxygen. Dinse *et. al.* showed that the C_2H_4 oxidation rate constant decreases upon a 50% reduction of VO_x, whereas rate constants associated with C_2H_6 ODH and oxidation remain unaffected [36]. This result is consistent with the proposed Scheme 2 which suggests that C_2H_6 only reacts with lattice oxygen and that C_2H_4 reacts with chemisorbed oxygen. During reoxidation, Scheme 2 proposes that bulk phase O_2 fills non-lattice vacancies, forming chemisorbed oxygen that subsequently fills lattice vacancies. Therefore, reducing the catalyst by 50% as done by Dinse *et. al.* would primarily remove the chemisorbed oxygen thereby reducing C_2H_4 overoxidation rates [36]. In summary, Scheme 2 captures the main trends presented in this and other works [32][36]. Further investigation is needed to fully understand why chemisorbed and lattice oxygen species participate exclusively in these specific reactions.

Table 2 summarizes these rates, rate expressions and kinetic parameters used in this study. As detailed in previous works, the kinetic parameters were fit to the 0.3mm catalyst which was verified to be absent of heat and mass transfer limitations [32].

Table 2: Reactions, rate expressions and kinetic parameters for the 3wt% VO_x Al_2O_3 catlayst used in this study.

Reaction	**Rate Expression** $\left[\frac{\mu mol}{mg-cat*min}\right]$	**3wt% VO_x**
Chemisorbed (O_*)		
$C_2H_4 + 4O_* \rightarrow 2CO_x + 2H_2O$	$k_3[C_2H_4][O_*]$	7.32e-3
$O_2 + 2* \rightarrow 2\,O_*$	$k_5[O_2][*]^2$	6.30-3
$O_* + L \rightarrow * + O_L$	$k_6[O_*][L]$	1.47e-4
Lattice (O_L)		
$C_2H_6 + O_L \rightarrow C_2H_4 + H_2O$	$k_1[C_2H_6][O_L]$	6.28e-3
$C_2H_6 + 5O_L \rightarrow 2CO_x + 3H_2O$	$k_2[C_2H_6][O_L]$	5.33e-4
$C_2H_4 + 4O_L \rightarrow 2CO_x + 2H_2O$	$k_4[C_2H_4][O_L]$	4.00e-3

The Scheme 2 kinetic model and Table 2 kinetic parameters are incorporated into the reactor model. We start by describing the reactor mass balances. The dimensionless gas phase species balances account for accumulation and convection:

$$\frac{\partial \boldsymbol{u_g}}{\partial \tau} = -\frac{\partial \boldsymbol{u_g}}{\partial \gamma} + \alpha\left(\boldsymbol{u_s}|_{\xi=1} - \boldsymbol{u_g}\right) \tag{29}$$

where

$$\boldsymbol{u} = \begin{bmatrix} u_{C_2H_6} \\ u_{O_2} \\ u_{C_2H_4} \\ u_{CO_x} \end{bmatrix} \tag{30}$$

The solid phase balance accounts for accumulation, diffusion and reaction within the catalyst pellets:

$$\frac{\partial \boldsymbol{u_s}}{\partial \tau} = \left(\frac{1}{\xi^2}\left(\frac{\partial}{\partial \xi}\xi^2 \frac{\partial \boldsymbol{u_s}}{\partial \xi}\right) - \overline{\overline{\boldsymbol{\phi}}}\,\widetilde{\boldsymbol{R}}\right) * \frac{1}{\beta} \tag{31}$$

The rates $\widetilde{\boldsymbol{R}}$, functions of the chemisorbed ($O*$) and lattice (O_L) oxygen consumption, are balanced by accumulation, assuming an absence of surface diffusion:

$$\frac{\partial \boldsymbol{\theta}}{\partial \tau} = -\overline{\overline{\boldsymbol{\psi}}}\,\widetilde{\boldsymbol{R}} \tag{32}$$

where $\boldsymbol{\theta}$ is the vector of surface coverages of chemisorbed and lattice oxygen:

$$\boldsymbol{\theta} = \begin{bmatrix} \theta_{O_*} \\ \theta_{O_L} \end{bmatrix} \tag{33}$$

The rates are determined from the reactions proposed in Scheme 2. Specifically, C_2H_6 reacts with O_L to produce C_2H_4. C_2H_4 may then be further oxidized to CO_x via $O*$ and O_L. Chemisorbed vacancies (*) are filled via dissociative adsorption of gaseous O_2. $O*$ may then fill lattice vacancies. The vector of these rates in dimensionless form is given by eqn. (34):

$$\widetilde{\boldsymbol{R}} = \begin{bmatrix} u_{C_2H_6}\theta_{O_L} \\ u_{C_2H_6}\theta_{O_L} \\ u_{C_2H_4}\theta_{O_*} \\ u_{C_2H_4}\theta_{O_L} \\ u_{O_2}\left(1-\theta_{O_*}\right)^2 \\ \theta_{O_*}\left(1-\theta_{O_L}\right) \end{bmatrix} \tag{34}$$

The gas phase boundary condition (BC) models a smoothed square wave aimed to mimic experimental FDO feeds as described in S15 in the presence of axial dispersion [48]:

$$\boldsymbol{u_g}(\gamma = 0, \tau \geq 0) = \frac{\boldsymbol{u_g^{Amp}}}{\tan^{-1}\left(\frac{1}{\delta}\right)} \tan^{-1}\left(\frac{\sin\left(\tilde{f}\tau + \boldsymbol{\varphi}\right)}{\delta}\right) + \boldsymbol{u_g^{Avg}} \tag{35}$$

The solid phase BCs respectively account for no flux at the center of the symmetric pellet and diffusion through a boundary layer surrounding the catalyst pellet:

$$\left.\frac{\partial \boldsymbol{u_s}}{\partial \xi}\right|_{\xi=0,\tau} = \boldsymbol{0} \tag{36}$$

$$\left.\frac{\partial \boldsymbol{u_s}}{\partial \xi}\right|_{\xi=1,\tau} = \overline{\overline{\boldsymbol{Sh}}}\left(\boldsymbol{u_g} - \boldsymbol{u_s}\right) \tag{37}$$

The initial conditions (ICs) consider the catalyst pre-treated and therefore fully oxidized at beginning of the experiment:

$$\boldsymbol{u_g}(\gamma > 0, \tau = 0) = \boldsymbol{u_s}(\xi, \tau = 0) = \boldsymbol{0} \tag{38}$$

$$\theta_{O_*}(\xi, \tau = 0) = \theta_{O_L}(\xi, \tau = 0) = 1 \tag{39}$$

The model was non-dimensionalized by introducing the following parameters. Further details on the dimensionless groups, transport parameters and equations including their dimensional form are detailed in sections S16, S17 and S18, respectively.

$$\tau = \frac{tF}{\varepsilon_b V_{tot}}; u_{g,i} = \frac{C_{g,i}}{C_{g,C_2H_6}^{Avg}}; \gamma = \frac{V}{V_{tot}}; \alpha = \frac{a_v k_g V_{tot}}{F}; \xi = \frac{r}{r_p};\ \beta = \frac{F\varepsilon_p r_p^2}{V_{tot}\varepsilon_b D_{eff}}; \phi_i$$

$$= \frac{r_p^2 \rho_{cat} k_i C_j}{D_{eff}}; \psi_i = \frac{V_{tot}\rho_{cat}\varepsilon_b k_i C_j}{F}; \tilde{f} = \frac{2\pi f \varepsilon_b V_{tot}}{F}$$

The Thiele moduli matrix is defined as:

$$\overline{\overline{\boldsymbol{\phi}}} = \begin{bmatrix} \phi_{C_2H_6,1} & \phi_{C_2H_6,2} & 0 & 0 & 0 & 0 \\ 0 & 0 & 0 & 0 & \phi_{O_2,5} & 0 \\ -\phi_{C_2H_4,1} & 0 & \phi_{C_2H_4,3} & \phi_{C_2H_4,4} & 0 & 0 \\ 0 & -2\phi_{CO_x,2} & -2\phi_{CO_x,3} & -2\phi_{CO_x,4} & 0 & 0 \end{bmatrix} \tag{40}$$

Following Scheme 2, rates for the surface balances are described by eqn. (41):

$$\overline{\overline{\boldsymbol{\psi}}} = \begin{bmatrix} 0 & 0 & 4\psi_{O_*,3} & 0 & -2\psi_{O_*,5} & \psi_{O_*,6} \\ \psi_{O_L,1} & 5\psi_{O_L,2} & 0 & 4\psi_{O_L,4} & 0 & -\psi_{O_L,6} \end{bmatrix} \tag{41}$$

The dimensionless system of partial differential equations (PDE's) is solved using the methods of lines (MOL) by discretizing the balances in the two spatial directions (γ and ξ). We used 25 and 6 cells for the axial and radial directions, respectively. The LSODA algorithm in Python was deployed to integrate dimensionless time (τ) the set of discretized equations. Since concentrations change along the length of the catalyst bed, the solid phase balance (eqn. 31) was

re-evaluated at each discretized point, resulting in a total of 150 ordinary differential equations (ODE's) per species in **u**. Further details on the discretization and evaluation of PDE's can be found in S19.

Kinetic parameters were obtained by fitting kinetically controlled 0.3mm catalyst pellets to step change experiments from our previous work [32]. These fits were performed by fitting ODH, combustion and oxygen transfer rate constants to step changes in the C_2H_6 concentration. After reduction, the catalyst was purged with N_2 and subsequently reoxidized to measure the reoxidation rate constants. Again, the 0.3 mm kinetic catalyst used in these fittings was confirmed to be absent of heat and mass transfer limitations [32]. The parameters for ethylene overoxidation rates in this study were manually tuned to capture yields observed at higher residence times using the 1.85 mm pellet. A comparison between parameters used in this study and in the originally fit ones are included in S18. Figs. 5, 8 and 10 of this study are all validations of the model; i.e., no adjustments were made in the parameter values. Other phenomena such as intracrystalline oxygen diffusion were also considered for this system as has been done by several others in the literature [29][50-53]. However, comparisons between reaction rates and diffusion time scales provided in S20 show that intracrystalline oxygen diffusion has a minimal influence on reaction rates, thereby permitting the use of eqn. (32) to describe generation and consumption of stored oxygen [29][32][50-53]. The 2-oxygen model was confirmed to be 0^{th} order in oxygen within the experimental conditions presented in this study, which is consistent with previous works in the literature [5][7-8][23][32]. Apparent oxygen orders of the 2-oxygen model were determined by solving the site balances analytically at SS as shown in S21.

We note that a single site oxygen model was also considered for this system. However, a single shared oxygen pool between C_2H_6 and C_2H_4 demonstrates minimal differences between

SSO and FDO. For this reason, the 2-oxygen model, which has firm mechanistic underpinnings, is necessary to explain the data. Further discussion of these points can be found in S22.

It is important to highlight the concern for heat transfer limitations potentially present with the larger catalyst pellets. To this end, heat transfer limitations at the pellet scale were assessed in section S13 by solving the energy balance in tandem with eqns. (29)-(41) above. Section S13 reports a maximum temperature rise of 6K early in the FDO reduction half cycle for the 2.6 mm catalyst pellets, thereby suggesting negligible heat effects. A maximum temperature difference of 4K was found between the bulk phase and pellet surface, thereby indicating minimal influence of interphase temperature gradients. Finally, intrapellet temperature profiles appear independent of pellet radius for all times throughout the reduction half cycle. This result indicates there are no intrapellet temperature gradient effects. Axial reactor hot spots were experimentally investigated by measuring the effluent temperature of different sized beds with equivalent gas flowrates. These results showed temperature increasing monotonically with bed length to a maximum rise of 6°C which is very similar to the model estimated value. This approach to measuring temperature profiles is only valid if thermal back-mixing is considered negligible [16]. The heat Peclet number for this system, evaluated from following work by Chen *et. al.* was found to be 26, thereby indicating minimal thermal back-mixing [16]. Finally, the SS isothermal analytical solution derived in section 3.1 and model were validated across feeds ranging from 1-3% C_2H_6 (at SSO) using a separate 10wt% VO_x catalyst (which has higher rates and thus greater heat transfer limitations). Validation at higher C_2H_6 concentrations over a more active catalyst further indicates minimal temperature effects at conditions used in this study. These collective results lead to the conclusion that the system can be considered isothermal and absent of heat transfer limitations. It is important to note that this model is developed around a lab scale reactor and that future works

focusing on industrial scale and associated higher ethane feed concentrations would certainly require more detailed considerations of heat effects on reactor performance.

Following the discussion on transport limitations, it is important to acknowledge the effect of large particle size on fluid dynamics. Specifically, the large pellet to diameter ratio (being 0.65 for the 2.6mm pellets) may disrupt flow patterns and result in reactant bypassing, poorer heat transfer, among other effects. This would require more extensive computational methods (i.e. computational fluid dynamics or CFD) to compute accurate flow profiles. Regardless, Figs. 5, 8 and 10 show good agreement between model and experiment across all pellet sizes without considering changes in flow patterns, suggesting negligible contributions of changes in flow patterns.

Reactor model results obtained from model eqns. (29-41) for SSO and FDO are compared with experimental data. The model was assessed under SSO by setting the amplitude in eqn. (32) to 0. Figs. 3A-D show that the model reproduces the negatively-sloped selectivity versus conversion during SSO and FDO. Furthermore, the model predicts decreasing C_2H_4 selectivity with increasing pellet size for fixed C_2H_6 conversion. This SSO trend is attributed to the longer diffusion path increasing the likelihood of the intermediate C_2H_4 overoxidation to CO_x. Furthermore, the model shows good agreement with the analytical solution derived in section 3.1 during SSO for all pellet sizes. Interestingly, the model also predicts the increasing gap between the C_2H_4 selectivity under FDO compared to SSO when using larger catalyst pellets.

With the model validated across the range of catalyst pellet sizes, we now apply the model to explore and understand the differences between FDO and SSO. Figs. 5A-D shows the dimensionless effluent concentrations versus dimensionless time for 0.3, 0.9, 1.85, and 2.6 mm pellets, respectively, over an entire cycle. [The O_2 concentration is scaled by a factor of 0.1 to fit

on the same axis.] It is especially revealing to examine the predicted species concentrations during the reduction half cycle. Note that since the C_2H_6 conversion decreases with increasing pellet size, the reactor residence times were adjusted so that each case has the same cycle-averaged C_2H_6 conversion (~16%); the residence times from smallest to largest pellet are as follows: 0.07 s, 0.079 s, 0.083 s, and 0.092 s.

Figs. 5A-D show that the O_2 concentration reaches SS much more rapidly during reoxidation than C_2H_6 does during reduction. Such trends for VO_x catalysts have been previously reported [5][7][32][53]. Figs. 5A-D also show subtle changes in the shapes of the product (C_2H_4, CO_x) concentration profiles as the pellet diameter increases. In particular, the C_2H_4 peak flattens out at early reduction times with increasing pellet size. This feature, coupled with the increase in CO_x, reveals that C_2H_4 produced early in the reduction cycle is overoxidized to CO_x. As mentioned earlier in sections 3.1-2, a larger diffusion length increases the extent of C_2H_4 overoxidation to CO_x, resulting in a lower C_2H_4 selectivity at the same C_2H_6 conversion.

In addition to the elevated CO_x concentrations early in the reduction half cycle, a new trend emerges during the latter portion of the reduction. Figs. 5A-D clearly show for each of the pellet sizes the effluent C_2H_4 concentration decreases more gradually than the CO_x concentration with time. This trend eventually results in the C_2H_4 concentration exceeding the CO_x concentration. Similar trends in C_2H_4 and CO_x concentrations were reported by Dinse *et. al.* when reducing a VO_x catalyst with C_2H_6 [39]. The trend indicates that the C_2H_4 point selectivity (instantaneous C_2H_4 concentration) increases with reduction time. On the other hand, it is further noted that reactant and product profiles respectively increase and decrease with time during the reduction half cycle, indicating a decreasing instantaneous C_2H_6 conversion with time. A lower C_2H_6 conversion with time is a consequence of depletion of $O*$ and O_L in the absence of gas phase O_2. In summary,

increasing reduction time decreases conversion and increases selectivity, much like decreasing residence time for consecutive reactions. We will expand on this trend in the subsequent section.

3.5: Evolution of chemisorbed (O_*) and lattice (O_L) oxygen:

The relationship between reduction time and reactor residence time has roots in the evolving O_*:O_L ratio within the catalyst bed for a kinetically controlled catalyst during C_2H_6 ODH [32]. Thus, in this case it is helpful to investigate the effects of reduction time on processes not only controlled by kinetics but those that are also controlled by diffusion. To illustrate, we follow the evolution of selective (O_L) and unselective (O_*) – tentatively assigned as lattice and chemisorbed oxygen species, respectively – within the catalyst bed during reduction and oxidation half cycles in FDO, and then compare these to SSO.

Recall that with Scheme 2 reactions involving C_2H_6 occur over lattice (O_L) oxygen whereas reactions involving C_2H_4 may occur over both lattice and chemisorbed (O_*) oxygen species. In sections 3.1-2 we showed that CO_x production is dominated by C_2H_6 and C_2H_4 oxidation under kinetic and mass transfer limited regimes, respectively. Taken together, these features suggest that varying the pellet size alters the oxygen species that is primarily consumed during CO_x production. Specifically, at low C_2H_6 conversion (<10%), kinetic and diffusion-controlled pellets are more inclined to consume O_L and O_*, respectively, when producing CO_x.

Previous sections showed that a higher C_2H_4 selectivity may be achieved during FDO compared to SSO in the presence of intraparticle diffusion limitations. Furthermore, the pellet size impacts the dominant route of CO_x production and, consequently, the specific oxygen species consumed (O_* vs. O_L). Fig. 6A plots the model-predicted ratio of chemisorbed to lattice oxygen (O_*:O_L) as a function of dimensionless time for the same four smaller size catalyst pellets from the experiments. As before, a complete cycle spanning the reduction and oxidation cycles is shown for

each. Since the O∗ and O_L concentrations vary within catalyst pellets and throughout the reactor, Fig. 6A reports the integral average of the O∗:O_L ratio, denoted as Ω throughout the pellets and reactor, according to:

$$\Omega \equiv \frac{O_{*,Avg}(\tau)}{O_{L,Avg}(\tau)} = \frac{\int_0^1 \int_0^1 \theta_{O_*}(\tau,\gamma,\xi)d\xi\, d\gamma}{\int_0^1 \int_0^1 \theta_{O_L}(\tau,\gamma,\xi)d\xi\, d\gamma} \tag{42}$$

To understand the evolution of O∗:O_L along the length of the bed, a second ratio averaged over the pellet and reduction time was plotted in Fig. 6B and is defined as:

$$\omega \equiv \frac{O_{*,Avg}(\gamma)}{O_{L,Avg}(\gamma)} = \frac{\int_{\tau_{0,red}}^{\tau_{f,red}} \int_0^1 \theta_{O_*}(\tau,\gamma,\xi)d\xi\, d\tau}{\int_{\tau_{0,red}}^{\tau_{f,red}} \int_0^1 \theta_{O_L}(\tau,\gamma,\xi)d\xi\, d\tau} \tag{43}$$

Before discussing the profiles during FDO, it is helpful to examine the O∗:O_L ratios (Ω and ω) during SSO. Figs. 6A and B show that during SSO, the time independent Ω and spatially dependent ω decrease with increasing pellet size. This implies that increasing pellet size results in a lower concentration of unselective O∗ relative to selective O_L. This trend is easily rationalized by the reactions in Scheme 2 which suggest that the primary (C_2H_6 ODH and combustion) and secondary (C_2H_4 combustion) reactions occur over O_L and O∗, respectively. With the feed free of intermediate C_2H_4, dominant reactions involve C_2H_6 ODH and oxidation, both of which consume lattice oxygen (see Scheme 2), thereby decreasing O_L without significantly affecting O∗. In other words, an absence of C_2H_4 in the feed means that O∗ consumption does not proceed as rapidly as that of O_L, resulting in Ω and ω exceeding unity. Furthermore, reoxidation and reduction rates of O∗ species are found to be higher than those for oxygen migration from the surface to the lattice [32]. This high turnover of O∗ therefore limits its ability to fully saturate lattice vacancies, also resulting in Ω greater than unity. However, as detailed in sections 3.1-2, increasing catalyst pellet size results in higher C_2H_4 oxidation rates due to trapping within the catalyst pellet, subsequently increasing

$O*$ consumption. Therefore, this effect is responsible for the decreasing Ω and ω with increasing pellet size during SSO.

Figs. 6A and B show significant differences between Ω and ω during SSO and FDO, especially during the reduction half cycles. Fig. 6A shows Ω for the 0.3 mm catalyst pellet to have an initial increase in Ω as a function of dimensionless time followed by a maximum and subsequent decrease. The initial Ω increase is a result of O_L being consumed by C_2H_6 ODH and oxidation, leaving behind $O*$, as similarly encountered during SSO. As the catalyst is further reduced in the absence of O_2, lattice vacancies begin to form, resulting in a higher driving force for $O*$ migration from the surface to the lattice, hence the subsequent decrease in Ω ratio. For larger pellets in Fig. 6A, the Ω maximum goes away, to be replaced by a monotonic decrease in Ω. This decrease is a result of higher C_2H_4 overoxidation rates caused by slower C_2H_4 diffusion out of the catalyst pellet thereby consuming $O*$ more rapidly with time resulting in lower $O*$:O_L ratios (Ω). Similarly, Fig. 6B shows ω to decline with pellet size earlier in the reactor which is consistent with C_2H_4 trapping in larger pellets thereby reducing $O*$ concentrations. Therefore, FDO of larger pellets generates a more significant disparity between ω earlier in the reactor thereby leading to FDO selectivities that are higher than SSO. This is important as this effect is not captured by Fig. 6A due to averaging over the entire bed. Therefore, if the average used in for Fig. 6A (eqn. 42) was terminated at a dimensionless distance earlier than 0.4, there would be more significant differences in the ratios with pellet size presented in Fig. 6A. As will be demonstrated later, this rapid change in ω earlier in the reactor in larger pellets will lead to higher degrees of selectivity enhancement during FDO.

Ultimately, and importantly, Figs. 6A and B suggest that FDO suppresses the unselective to selective oxygen ratios (Ω and ω), resulting in higher C_2H_4 selectivities. The absence of gas phase O_2 during the reduction half cycle leaves * vacancies unfilled after $O*$ is either consumed

by C_2H_4 or lattice vacancies. Figs. 3A-D indeed show that larger pellet sizes exhibit a decreasing C_2H_4 selectivity during FDO. Thus, by accelerating the removal O_* and preventing reoxidation of unselective (*) sites during the reduction half cycle, FDO can reduce the amount of C_2H_4 lost to CO_x, especially in larger catalyst pellets. Conversely, the sustained SSO supply (as opposed to intermittent FDO supply) of O_2 results in refilling of unselective vacancies. This leads to a more rapid decrease in C_2H_4 selectivity with increasing pellet size (Figs. 3A-D). As mentioned previously, O_* and O_L profiles differ based on the reactor and pellet location, thereby requiring the use of an integral average (Ω) over the pellets and bed to understand the evolution with time or (ω) over the pellets and reduction time to understand the evolution across the bed. An examination of the intrapellet temporal evolutions of conversion, selectivity, and the O_*:O_L ratio are included in S23. As will be demonstrated in the following section, selectivity enhancement can be further understood and optimized by tracking its instantaneous as opposed to its cycle average values.

3.6: Cycle periods and deviations from SSO selectivity conversion curves during FDO.

It is interesting to examine and compare the C_2H_4 selectivity versus C_2H_6 conversion during FDO and SSO. Figs. 3A-D shows that these follow separate trajectories with the gap between them widening with increasing pellet size; i.e., stronger intrapellet diffusion limitations (Fig. 3). Our previous work showed that increasing cycle period results in higher C_2H_4 selectivity and lower C_2H_6 conversion while remaining on the same selectivity-conversion curve for kinetically controlled pellets for a range of periods [32]. It is helpful to consider the C_2H_4 selectivity enhancement ($\Delta S_{C_2H_4}$) between FDO (S_{FDO}) and SSO (S_{SSO}) at the same C_2H_6 conversion ($X_{C_2H_6}$), defined as follows:

$$\Delta S_{C_2H_4}\left(\tau, X_{C_2H_6}\right) = S_{FDO}\left(\tau, X_{C_2H_6}\right) - S_{SSO}\left(X_{C_2H_6}\right) \quad (44)$$

The dependence of $\Delta S_{C_2H_4}$ on dimensionless pellet position ξ for different dimensionless times is plotted in Figs. 7A and B for 0.3 and 2.6 mm catalyst pellets, respectively. Fig. 7A shows that $\Delta S_{C_2H_4}$ has a maximum value of 12% at $\tau = 414$. At longer time ($\tau = 1259$), $\Delta S_{C_2H_4}$ falls back to a value of 7.5% and the enhancement short-lived. This trend suggests that shorter reduction times, operationally obtained by using smaller periods, would result in higher selectivity enhancement for the kinetically controlled pellet. Subsequent paragraphs will discuss this further.

The selectivity enhancement profiles for the 2.6 mm pellet plotted in Fig. 7B reveal a considerably larger enhancement during FDO. [Note the difference in axes between Figs. 7A and B.]. In contrast to the 0.3 mm pellet (Fig. 7A), the 2.6mm pellet (Fig. 7B) has a monotonic increasing selectivity enhancement with time suggesting that it increases with reduction time. As stated previously, increasing reduction time would be achieved by increasing the cycle period. Thus, 0.3 and 2.6 mm pellet selectivity differences are maximized by small and large periods, respectively. This will be discussed in more detail later.

With a deeper understanding transient reaction and diffusion occurring within the catalyst pellets, one can further investigate its effect on the reactor gas (bulk) phase by monitoring the instantaneous C_2H_4 selectivity and C_2H_6 conversion during the reduction half cycle. Data points in Figs. 8A-D plot, for each of the pellet sizes, the instantaneous C_2H_4 selectivity during the reduction half cycle as a function of conversion at the reactor outlet predicted by the model and measured experimentally. Additional figures containing moving averages of data points are included in S24. Starting at the beginning of a reductive cycle (denoted by larger open triangles in each figure), with increasing time during the reduction half cycle the instantaneous C_2H_4 selectivity and C_2H_6 conversion increase and decrease, respectively. Following earlier results, these trends are a consequence of diminishing stored oxygen consumed by reaction in the absence

of O_2 during the reduction. Fig. 8A shows that the difference between C_2H_4 selectivity achieved during FDO and SSO (red solid line) is greatest at intermediate reduction times. This is consistent with the largest selectivity enhancement encountered early in the half cycle (Fig. 7A). Collectively, the findings of Figs. 7A and 8A suggest that the largest enhancement is gained through periodic operation at intermediate frequency for 0.3 mm pellets. Lower frequencies during FDO do not provide a significant enough increase in selectivity between the beginning (60%) and end (90%) of the half cycle to outperform SSO. This point, coupled with the decrease in C_2H_6 conversion, results in a moving average C_2H_4 selectivity that converges towards SSO selectivities (see section S24). Higher frequencies do not allow a significant enough time for the O_*:O_L ratio to decrease leading to similar FDO and SSO solutions.

The exact opposite trend is observed for diffusion-controlled catalysts in Figs. 8B-D. Figs. 8B-D show that larger differences between FDO and SSO selectivities occur at later times in the cycle. Specifically, the results show that with increasing time, the difference between FDO and SSO selectivities increases. This difference becomes more pronounced in larger catalyst pellets. For instance, Figs. 8B-D show that the experimentally measured difference between selectivities in the initial and final portions of the reduction half cycle are 27, 34 and 37% for 0.9, 1.85 and 2.6 mm pellets, respectively. Thus, Figs. 8B-D suggest that longer periods when using larger catalyst pellets will result in larger differences between the FDO and SSO selectivities. It is well known that the effect of a periodic perturbation on a system is strongly dependent on the oscillation frequency and time scale of the system [32][54-59]. Since larger catalyst pellets are controlled by diffusion, which is slower than kinetics, a larger period (smaller frequency) is required to elicit larger deviations between SSO and FDO [32][54-59]. A more detailed discussion on modulation frequency and diffusion time scales will be discussed later.

Another interesting observation in Figs. 8A-D is the instantaneous C_2H_4 selectivities at the end of the reduction half cycle (low conversions). In Fig. 8A, the instantaneous C_2H_4 selectivities asymptotically approach 90% at long times (low conversions). In our previous work, we found the selectivity of primary reactions to be approximately 91% [32]. This finding, in conjunction with Fig. 8A, suggests that during FDO the reaction transitions from triangular to parallel in nature as $O*$ is depleted. However, the terminal selectivities of larger pellets (Figs. 8A-D) show that the C_2H_4 selectivity at the end of the reduction half cycle decreases with pellet size from 90% to 76%. Scheme 2 indicates that C_2H_4 overoxidation may occur over lattice oxygen. Thus, like the decline in selectivity during SSO with pellet size, this decline is also a result of higher C_2H_4 overoxidation rates induced by diffusion limitations utilizing lattice oxygen (as it is in more abundance than chemisorbed oxygen, Figs. 6A and B). Since C_2H_4 combustion rates over chemisorbed oxygen are nearly twice those over lattice oxygen, chemisorbed oxygen depletion would more significantly reduce the overall ethylene consumption, hence the elevated instantaneous C_2H_4 selectivities.

While instantaneous FDO selectivities are consistently higher than those achievable during SSO, cycle average FDO selectivities in the 0.3 mm catalyst pellet are nearly identical to SSO selectivities (Fig. 3A). Similarities between FDO and SSO selectivities in 0.3 mm pellets are a result of the simultaneous increase and decrease in the instantaneous C_2H_4 selectivity and C_2H_6 conversion, respectively. Therefore, as the catalyst is reduced, the instantaneous selectivity and conversion will increase and decrease, respectively (Figs. 8A-D). In Fig. 8A, the loss in conversion outweighs the gain in selectivity, leading to a cycle average value that is nearly identical to that achieved during SSO. This slower selectivity gain is rationalized by the slower evolution of the $O*$:O_L ratio (ω) with time in Fig. 6B. Furthermore, since the 0.3 mm catalyst pellet is nearly absent of diffusion limitations, C_2H_4 overoxidation rates do not play as significant of a role in selectivities

as they would in larger catalyst pellets. In other words, increasing the pellet size leads $O*$ to have a more dramatic effect on the overall selectivity. Thus, changes to the $O*:O_L$ ratio will more significantly influence selectivities of diffusion-controlled pellets due to higher C_2H_4 combustion rates compared to smaller pellets at equivalent conversions. This effect is captured in Figs. 8A-D which show that instantaneous selectivities change more drastically with reduction time as the catalyst pellet diameter increases. Specifically, the slope of instantaneous selectivity versus conversion increases with pellet size suggesting higher selectivity gains with smaller conversion losses as the pellet size increases. Again, this rapid selectivity increase is captured in Fig. 6B which shows a more rapid decline in ω with pellet size earlier in reactor for larger catalyst pellets. Thus, FDO enhancement is only observed when there is a significant change to the $O*:O_L$ ratio coupled with higher sensitivities of selectivity on the unselective oxygen species ($O*$), which in this case, are induced by diffusion limitations.

Figs. 8A-D also show that selectivities at earlier reduction times converge towards the SSO selectivity. It is well known that systems subjected to periodic perturbations (i.e. FDO) with frequencies higher than the response time of the system will produce results similar to SSO [32][55-59]. In this case, the differences between selectivity enhancement at smaller periods in Figs. 8A-D indicate that each pellet is governed by different time scales. For instance, a 2 min period was used during periodic operation for all pellet sizes despite each being governed by a combination of kinetics and diffusion. The large difference between C_2H_4 selectivities during SSO and beginning of the FDO cycle in 0.3 and 0.9 mm pellets (Figs. 8A-B) suggest that oscillations with these periods are still slower than the response time of the system. Therefore, even smaller periods are required for FDO selectivities to converge towards SSO selectivities, which are not attainable through this experimental set up. However, Figs. 8C-D show that 1.85 and 2.6 mm

pellets have instantaneous C_2H_4 selectivities during FDO that converge towards SSO selectivities with smaller periods. Therefore, the periods required to converge FDO and SSO selectivities are smaller for kinetically rather than diffusion controlled catalyst pellets. In summary, diffusion controlled catalyst pellets exhibit slow time scales than kinetically controlled pellets therefore requiring larger periods to achieve enhancement. This can be further demonstrated by investigation oscillation and diffusion time scales.

Figure 9 shows that the ratio of pellet residence and feed modulation times determined from the dimensionless parameters $\tilde{f} * \beta$ with pellet size. Different switching times were approximated by doubling the reduction time (i.e. the overall cycle is distributed equally between reduction and oxidation) which implies that the catalyst is assumed to return to its original oxidation state at the end of a cycle. This is a plausible assumption given that reoxidation is much faster than reduction thus the time required to refill vacancies will always be lower than the reduction time especially with significantly higher O_2 concentrations. Larger pellet sizes result in longer times required to diffuse throughout the catalyst pellet hence increasing the diffusion modulation time ratio. Furthermore, Figure 9 shows that the ratio between diffusion and modulation times increase with smaller periods (lower reduction times / conversions). Smaller periods (higher frequencies) during FDO imply the concentration at the reactor inlet is switching more rapidly with time. Such rapid perturbations eventually approach the time required for gases to diffuse through the catalyst pellet thereby increasing the ratio at smaller periods. As described in the main text and previous works [32][55-59], modulations during FDO that approach the characteristic time of the system result in FDO performances that converge towards SSO. Figs. 8 and 9 illustrate this effect in the 1.85 and 2.6 mm catalyst pellets early into the reduction half cycle. It is important to note that the diffusion to switching time ratios for 0.3 and 0.9 mm pellets do not

reach unity like the larger pellets at higher conversions. This is also reflected in Fig. 8 as the experimentally measured selectivities do no lie on the SSO selectivity curve. This is likely a result of diffusion and kinetics being faster than the time at which the MS can sample data. Thus, if the MS were capable of sampling data more rapidly, there would be more similarities between FDO and SSO selectivities earlier in the reduction half cycle for 0.3 and 0.9 mm pellets. Also mentioned previously is the relationship between modulation frequency and C_2H_6 conversion. For instance, higher frequencies during FDO imply that the catalyst remains at a higher oxidation state (higher concentration of stored oxygen) due to smaller reduction times subsequentially resulting in higher C_2H_6 conversions. Therefore, smaller periods result in higher ratios and C_2H_6 conversions as illustrated in Figure 9. Figure 9 shows that the ratio between diffusion and modulation time scales during FDO in the 1.85 and 2.6 mm catalyst pellets approach unity at low periods and roughly 25-30% C_2H_6 conversion. Finally, Figures 8A-D also show that C_2H_4 selectivity during FDO approaches that achieved during SSO at these C_2H_6 conversions. This observation paired with Figure 9 suggest that similarities between C_2H_4 selectivities during FDO and SSO are a consequence of similar modulation and diffusion time scales.

While larger periods result in the largest difference between FDO and SSO selectivities (Figs. 8B-D), they do not necessarily constitute the best mode of operation. Consider the instantaneous C_2H_4 selectivity achieved during FDO. Figs. 8A-D show simultaneously decreasing conversion and increasing selectivity with time (reduction time or cycle period). Considering the trade-off between selectivity and conversion in Figs. 8A-D, it is beneficial to investigate the C_2H_4 yield enhancement between FDO and SSO at the same C_2H_6 conversion as a function of time as described by:

$$\Delta Y_{C_2H_4}\left(\tau, X_{C_2H_6}\right) = Y_{FDO}\left(\tau, X_{C_2H_6}\right) - Y_{SSO}\left(X_{C_2H_6}\right) = \left[S_{FDO}\left(\tau, X_{C_2H_6}\right) - S_{SSO}\left(X_{C_2H_6}\right)\right] X_{C_2H_6} \quad (45)$$

Figs. 10A-D plots the experimentally measured and model predicted C_2H_4 yield difference between FDO and SSO for 0.3, 0.9, 1.85 and 2.6 mm catalyst pellets, respectively, during the reduction half cycle at different points in the reactor. Fig. 10A shows that the yield enhancement for the kinetically controlled 0.3 mm catalyst pellet is the highest at early times in the reduction half cycle. This agrees with previous observations in Figs. 7-8 which show that faster oscillations (smaller periods) result in larger FDO selectivity enhancement. Furthermore, the leftward skewness of the yield enhancement with time in Fig. 10A suggests that larger periods would rapidly decrease the cycle average yield enhancement. Interestingly, the experimentally measured maximum yield enhancement decreases from Fig. 10A to B with an increase in the catalyst pellet size from 0.3 mm to 0.9 mm. This decrease is followed by the migration of the maximum yield enhancement to later times in the reduction half cycle. As demonstrated earlier, the 0.3 mm pellet in Fig. 10A is kinetically limited and therefore the observed enhancement is likely a result of the kinetics in Scheme 2. In contrast, the larger pellet in Fig. 10B is influenced by both kinetics and intraparticle diffusion. Further evidence of this is seen in the growth and rightward shift of the second yield enhancement peak in Figs. 10C-D when increasing the catalyst pellet size to 1.85 mm and 2.6 mm, respectively. More specifically, diffusion being a slower process than kinetic phenomena would require more time to induce higher degrees of dynamic enhancement. Figs. 10C-D show that the maximum yield enhancement increases with pellet size. Furthermore, the peak shifts to the right with pellet size in Figs. 10A-D, this indicates that longer periods are required to induce this effect which is likely a consequence of longer diffusion length scales associated with the larger pellets. As seen in Figs. 10A-D these features are present in model and experimental results at similar points in time.

Figs. 10A-D indicate that larger catalyst pellets require longer periods to achieve higher C_2H_4 yields during FDO relative to SSO. Again, longer periods are required for larger pellets due to slower diffusion. Maxima in yield enhancement curves in Figs. 10A-D mark the point at which the reduction cycle should end to optimize cycle average yield differences between FDO and SSO. Thus, by plotting yield as a function of time during the reduction half cycle as is done in Figs. 9A-D one can determining switching times that maintain the largest difference between FDO and SSO. While this approach is demonstrated for ethane ODH, it can be extended to other reactions in which the desired yield exhibits similar trends with time.

4. Conclusions

Selectivities and yields towards desirable intermediate products in sequential catalytic reaction systems are often limited by the diffusion within catalyst pellets. In general, larger catalyst pellets have lower intermediate selectivity than small pellets. Through a combination of modeling and experiment, this work demonstrates that forced dynamic operation (FDO) of C_2H_6 oxidative dehydrogenation (ODH) reduces C_2H_4 overoxidation to CO_x in larger catalyst pellets when compared to steady state operation (SSO), thereby resulting in higher C_2H_4 FDO selectivities as a function of C_2H_6 conversion than those achieved via SSO. Unlike previous works, these results demonstrate the ability of FDO to reduce selectivity losses encountered during intrapellet diffusion limitations which is a prevalent issue at the industrial scale.

Experimental results confirmed the detrimental impact of diffusion limitations on selectivity during SSO. However, the selectivity losses may be reduced through FDO by reducing C_2H_4 overoxidation rates which are typically increased by its trapping within diffusion-controlled pellets. FDO of diffusion-controlled pellets result in higher C_2H_4 selectivities at the same C_2H_6

conversion despite all reactions being independent of oxygen concentration; which was previously found to be a criterion for lack of enhancement in FDO reactors, thereby making this a case of diffusion rather than kinetic enhancement. In this case, diffusion limitations in larger pellets make selectivities more sensitive to C_2H_4 combustion rates and subsequentially $O*$. Therefore, in the absence of gaseous O_2, diffusion-controlled pellets remain more selective during FDO through lower $O*:O_L$ ratios than SSO where reduction and oxidation occur simultaneously. Cycle periods during FDO can mimic changes in reactor residence time and can be tuned to further maximize yield differences between FDO and SSO.

This study provides a case of selectivity enhancement through FDO by mitigating selectivity losses via C_2H_4 combustion within diffusion controlled catalyst pellets. Furthermore, this study suggests that FDO enhancement can be further optimized through a careful tuning of modulation frequency and pellet transport properties. Ergo, this study prompts future investigations into the effects of other industrially significant transport phenomena including heat and momentum which may also play integral roles in the optimization and implementation of FDO in other selective oxidation processes.

Acknowledgements

The authors acknowledge support from the National Science Foundation (EFMA 2029359). One of the authors (MPH) is compensated for an advisory role for Omnis Energy Inc.

Notation List:

Letters
C = Concentration [μmol/cm^3]
Da = Damköhler Number
D_{eff} = Effective diffusion constant of species i
Ea = Apparent activation energy [kJ/mol]
F = Volumetric flow rate [cm^3/min]

M_i = Molar mass of species i [g/mol]
P = Pressure [atm]
R = Gas Constant [J/mol/K]
R_i = Rate of species i [μmol/mg-cat/min]
$\widetilde{\boldsymbol{R}}$ = Vector of dimensionless rates
Sc = Schmitt Number
Sh = Sherwood Number
T = Temperature [K]
V = Volume [cm^3]

a_i = Parameters used in the analytical solution defined as $a_1 = \frac{\eta'_3 \, Da_3}{\eta_1(Da_1+Da_2)}$ and $a_2 = \frac{(Da_3 \, \beta(\eta_1-\eta'_3)-\eta_1 Da_1)}{\eta_1(Da_1+Da_2)}$
f = Frequency [1/min]
k_g = Interfacial mass transfer coefficient [cm/min]
k_i = Rate constant of reaction i [min^{-1} for 1st order reaction and cm^3 μmol^{-1} min^{-1} for second order reactions]
$r_{i,b}$ = Rate in bulk phase [μmol/mg-cat/min]
r_p = radius of catalyst pellet [cm]
r = Radius [cm]
s = Duty cycle
t = Time [min]
u = Dimensionless concentration

Greek Letters:
α = Parameter defined as $\left(u_{b,C_2H_4} - y_1 - \left(\frac{Sh_1}{Sh_2}\right)\left(\beta \, u_{b,C_2H_6} - y_1\right)|_{\xi=1}\right)$ for the analytical solution and $\left(\frac{a_v k_g V_{tot}}{F}\right)$ for the numerical solution.

β = Parameter defined as $\left(\frac{\phi^2_{C_2H_4,1}}{\left(\phi^2_{C_2H_4,3}-\phi^2_{12}\right)}\right)$ for the analytical solution and $\left(\frac{F\varepsilon_p r_p^2}{V_{tot}\varepsilon_b D_{eff}}\right)$ for the numerical solution
δ = Parameter in differentiable square wave (sharpness)
θ = Normalized surface coverage
ε_i = Void fraction
η_i = Effectiveness factor of reaction i
φ = Phase shift
ρ_{cat} = Density of catalyst [mg cat/cm^3 bed]
ϕ = Thiele modulus
τ = Dimensionless time or tortuosity
ξ = Dimensionless distance in catalyst pellet
γ = Dimensionless distance in the reactor
ψ = Dimensionless rate constant
Ω = Ratio of reactor averaged chemisorbed (O_*) to lattice oxygen (O_L) normalized coverages.

ω = Ratio of pellet and reduction time averaged chemisorbed (O_*) to lattice oxygen (O_L) normalized coverages.

Subscripts:
Tot = Total
b = Bulk phase
p = pellet
eff = Effective
g = gas phase
s = solid phase

Superscripts:
Amp = Amplitude
Avg = Average
f = Feed
‘ = Of the uncoupled problem
° = Reference (Concentration)

References:

[1] Gärtner, C. A., van Veen, A. C., & Lercher, J. A., *Chem. Cat. Chem.* **11**, 3196–3217 (2013).

[2] Najari, S., Saeidi, S., Concepcion, P., Dionysiou, D. D., Bhargava, S. K., Lee, A. F., & *Chem. Soc. Rev.* **7**, 4564–4605 (2021).

[3] Skoufa, Z., Heracleous, E., & Lemonidou, A. A., *Chem. Eng. Sci.* **84**, 48–56 (2012).

[4] López, E., Heracleous, E., Lemonidou, A. A., & Borio, D. O., *Chem. Eng. J.*, **145**, 308–315 (2008).

[5] Argyle, M. D., Chen, K., Bell, A. T. & Iglesia, E., *J. Phys. Chem. B.* **106**, 5421–5427 (2002).

[6] Yao, R., Herrera, J. E., Chen, L., & Chin, Y. H. C., *ACS Catal.* **10**, 6952–6968 (2020).

[7] Argyle, M. D., Chen, K., Bell, A. T. & Iglesia, E., *J. Catal.* **208**, 139–149 (2002).

[8] Blasco, T., Galli, A., López Nieto, J. M., & Trifiró, F., *J. of Catal.*, **169**, 203–211 (1997).

[9] Martínez-Huerta, M. v, Gao, X., Tian, H., Wachs, I. E., Fierro, J. L. G., Bañares, M. A., & Sánchez, F., *Catal. Today* (2006).

[10] Hill, C. *An Introduction to Chemical Engineering Kinetics & Reactor Design*, John Wiley & Sons Inc. (1977)

[11] Smith, J. *Chemical Engineering Kinetics*, McGraw-Hill Book Company, 2nd edition (1970)

[12] Bennett, C., Myers, J., *Momentum, heat and mass transfer*, McGraw-Hill Book Company (1962)

[13] Rawlings, J., Ekerdt, J. Chemical Reactor Analysis and Design Fundamentals, Nob Hill Publishing (2004)

[14] Froment, G., Bishoff, K., De Wilde, J.*, Chemical Reactor Analysis and Design,* John Wiley & Sons Inc., 3rd edition (2011)

[15] Frank, B., Dinse, A., Ovsitser, O., Kondratenko, E. v., & Schomäcker, R. *Appl. Catal. A* **323**, 66–76 (2007).

[16] Chen, J., Sun, Z., Bollini, P., & Balakotaiah, V., *Chem. Eng. Sci.* **273**, (2023).

[17] Gao, Y., Neal, L. M., & Li, F., *ACS Catal.* **6**, 7293–7302 (2016).

[18] Novotný, P., Yusuf, S., Li, F., & Lamb, H. H., *Catal. Today* **317**, 50–55 (2018).

[19] Haddad, N., Bordes-Richard, E., Hilaire, L., & Barama, A., *Catal. Today* **126** (1–2), 256–263 (2007).

[20] Luongo, G., Donat, F., Bork, A. H., Willinger, E., Landuyt, A., & Müller, C. R., *Adv. Energy Mater.* **12** (2022).

[21] Yusuf, S., Neal, L., Haribal, V., Baldwin, M., Lamb, H. H., & Li, F. (2018). *Appl. Catal. B: Env.* **232**, 77–85 (2018).

[22] Bakare, I. A., Mohamed, S. A., Al-Ghamdi, S., Razzak, S. A., Hossain, M. M., & de Lasa, H. I. *Chem. Engi. J.* **278**, 207–216 (2015).

[23] Waku, T., D. Argyle, M., T. Bell, A. & Iglesia, E. *Ind. & amp; Eng. Chem. Res.* **42**, 5462–5466 (2003).

[24] Brody, L., Neal, L., Liu, J., & Li, F., *Energy Fuels* **36**, (2022).

[25] Neal, L. M., Yusuf, S., Sofranko, J. A., & Li, F., *En. Tech.*, **10** (2016).

[26] Novotný, P., Yusuf, S., Li, F. & Lamb, H. H., *J. Chem. Phys.* **152**, 044713 (2020).

[27] Harold, M. P., Zaspalis, V. T., Keizer, K., & Burggraaf, A. J. (1993). *Chem. Eng. Sci.*, **48**, 2705–2725.

[28] Haber, J., & Turek, W. J., *J. Catal.* **190**, 320–326 (2000).

[29] Huang, X.-F., Li, C.-Y., Chen, B.-H., & Silveston, P. L., *AIChE J.* **48**, 846–855 (2002).

[30] Heracleous, E., & Lemonidou, A. A., *Catal. Today* **112**, 23–27 (2006).

[31] Gabra, S., Baldoví, H. G., Williams, G., Poulston, S., & Dennis, J., *AIChE Annual Meeting, Conference Proceedings*, *2019-November*. (2019).

[32] Morales, A., Harold, M. P., and Bollini, P., *ACS Catal.* **14**, 7877-7892 **(**2024).

[33] Chen, P., Xie, Z., Zhao, Z., Liu, B., Fan, X., Kong, L., Xiao, X., *Mol. Catal.*, **535**, (2023).

[34] Ozkan, U. S., Smith, M. R., Driscoll, S. A., *J. Catal.*, **134**, (1992).

[35] Mills, P. L., Randall, H. T., McCracken, J. S., *Chem. Eng. Sci*, **54**, (1999).

[36] Creaser, D., Andersson, B., Hudgins, R. R., Silveston, P. L., *Chem. Eng. Sci.* **54**, 4437-4448 (1999).

[37] Gan, Z., Brazdil, J. F., Grabow, L. C., Epling,W. S., *App. Catal. A* **672**, 119585 (2024).

[38] Gebers, J.C., Harrison, A.R.P. & Marek, E.J. *Discov. Chem. Eng.* **2**, 4 (2022).

[39] Dinse, A., Schoma¨cker, R. S., & Bell, A. T., *Phys. Chem. Chem. Phys.* (2009).

[40] Khodakov, A., Yang, J., Su, S., Iglesia, E., & Bell, A. T. *J. Catal.* **177**, 343–351 (1998).

[41] Elbadawi, A. A. H., Ba-Shammakh, M. S., Al-Ghamdi, S., Razzak, S. A., & Hossain, M. M. *Chem. Eng. J.* **284**, 448–457 (2016).

[42] Schwarz, O., Frank, B., Hess, C., & Schomäcker, R., *Catal. Commun.* **9**, 229–233 (2008).

[43] J. Le Bars, A. Auroux, M. Forissier, J.C. Vedrine, *J. Catal.* **2**, 1996, 250-259 (1996).

[44] Cho, B. K., *Ind. Eng. Chem. Fund.* **22**, 410–420 (1983).

[45] Aleksandrov, A., Kolmogrorov, A., Lavrent'ev, A., Mathematics Its Content, methods, and Meaning, The M.I.T. Press, Vol. 3 (1956).

[46] Fanchi, J. Math Refresher for Scientists and Engineers, John Wiley & Sons Inc (1997).

[47] Boyce, W., DiPrima, R., Elementary Differential Equations and Boundary Value Problems, John Wiley & Sons, 3rd Edition (1965).

[48] Ting, A. W. L., Li, M., Harold, M. P., & Balakotaiah, V., *Chem. Eng. J.*, **326**, 419–435 (2017).

[49] van der Linde, S. C., Nijhuis, T. A., Dekker, F. H. M., Kapteijn, F., & Moulijn, J. A., *App. Catal. A* **151**, 27–57 (1997).

[50] Redlingshöfer, H., Fischer, A., Weckbecker, C., Huthmacher, K., & Emig, G. *Ind. Eng. Chem. Res.*, **42**, 5482–5488 (2003).

[51] Zhou, Z., Harold, M. P., & Luss, D., *Ind. and Eng. Chem. Res.*, **60**, 6465–6482 (2021).

[52] Kapoor, R., & Oyama, S. T., *J. Mater. Res.* **2**, (1997).

[53] Hwang, A., Wu, J., Getsoian, A. "Bean," & Iglesia, E., *J. Phys. Chem. C* **127**, 2936–2952 (2023).

[54] Sinčić, D., & Bailey, J. E., *Chem. Eng. Sci.* **35**, 1153–1161 (1980).

[55] Silveston, P. L., & Hudgins, R. R., *Periodic Operation of Chemical Reactors*. Elsevier Science. (2013).

[56] Silveston, P., Hudgins, R. R., & Renken, A., *Catal. Today* **25**, 91–112 (1995).

[57] Lee C K, & Bailey James E., *Ind. Eng. Chem. Process Des. Dev.* **19**, (1980).

[58] Petkovska, M., Nikolić, D., & Seidel-Morgenstern, A., *Isr. Journal of Chem.* **58** (6–7) (2018).

[59] Sterman, L. E., & Erik Ydstie, B., *Chem. Eng. Sci.*, **45**, 721–736 (1990).

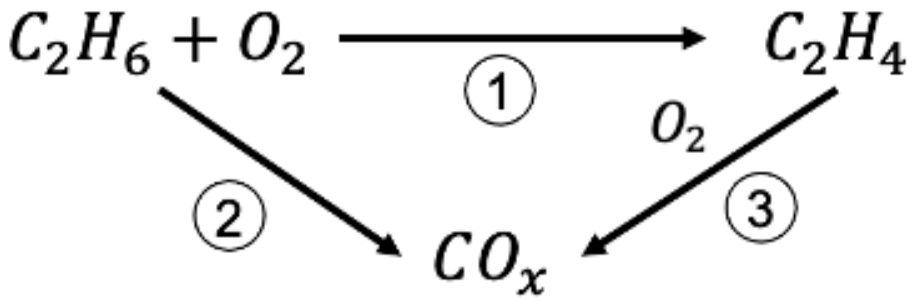

Scheme 1: Reaction pathways present during C_2H_6 ODH over VO_x catalyst.

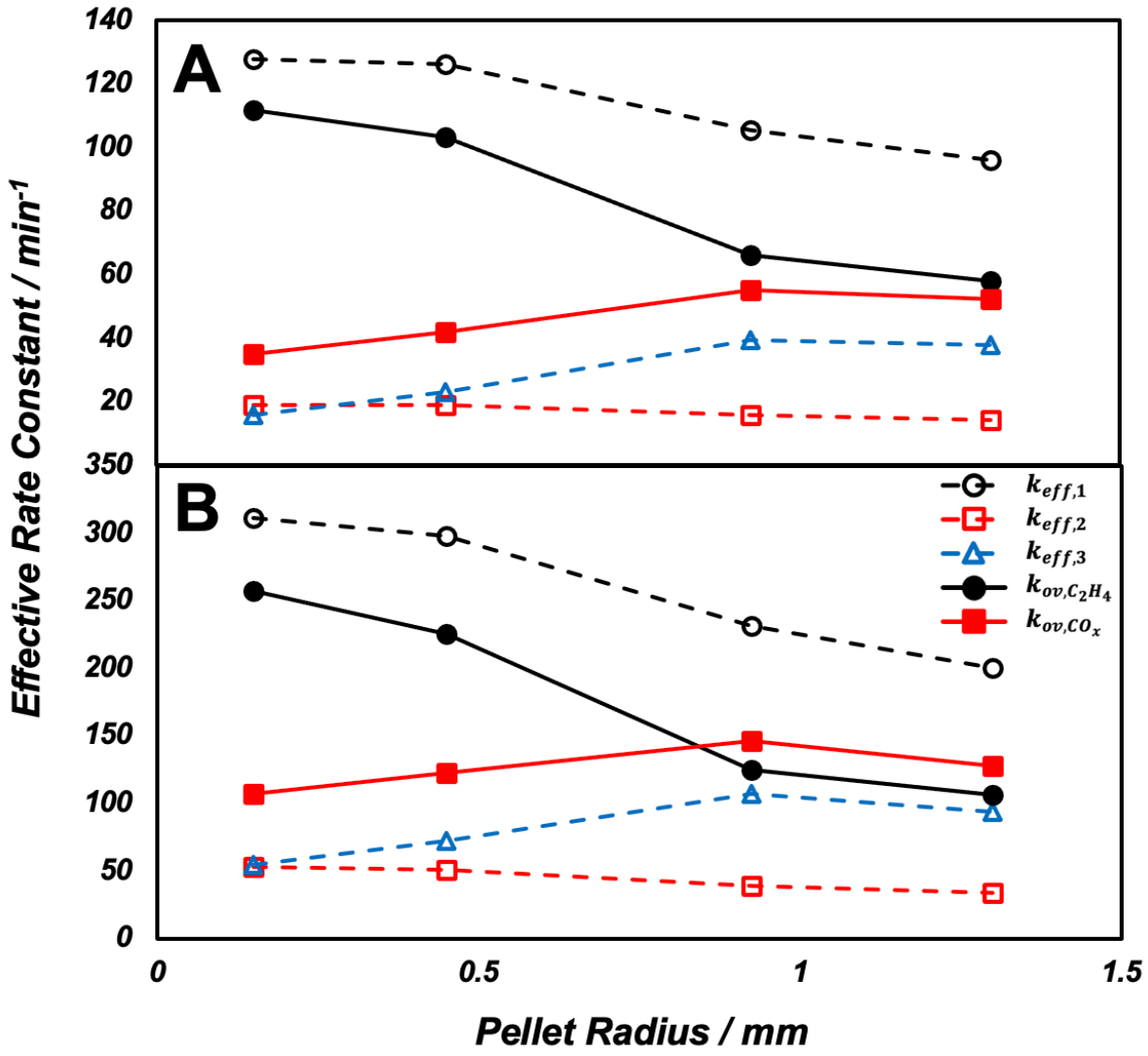

Figure 1: Effective rate constants of steps 1-3 in scheme 1 eqns. (27-29) and of overall C_2H_4 and CO_x formation rates defined by eqns. (25-26) as a function of pellet radius at 500 (A) and 550°C (B) estimated at 0.5 mg sccm^{-1} from the analytical solution.

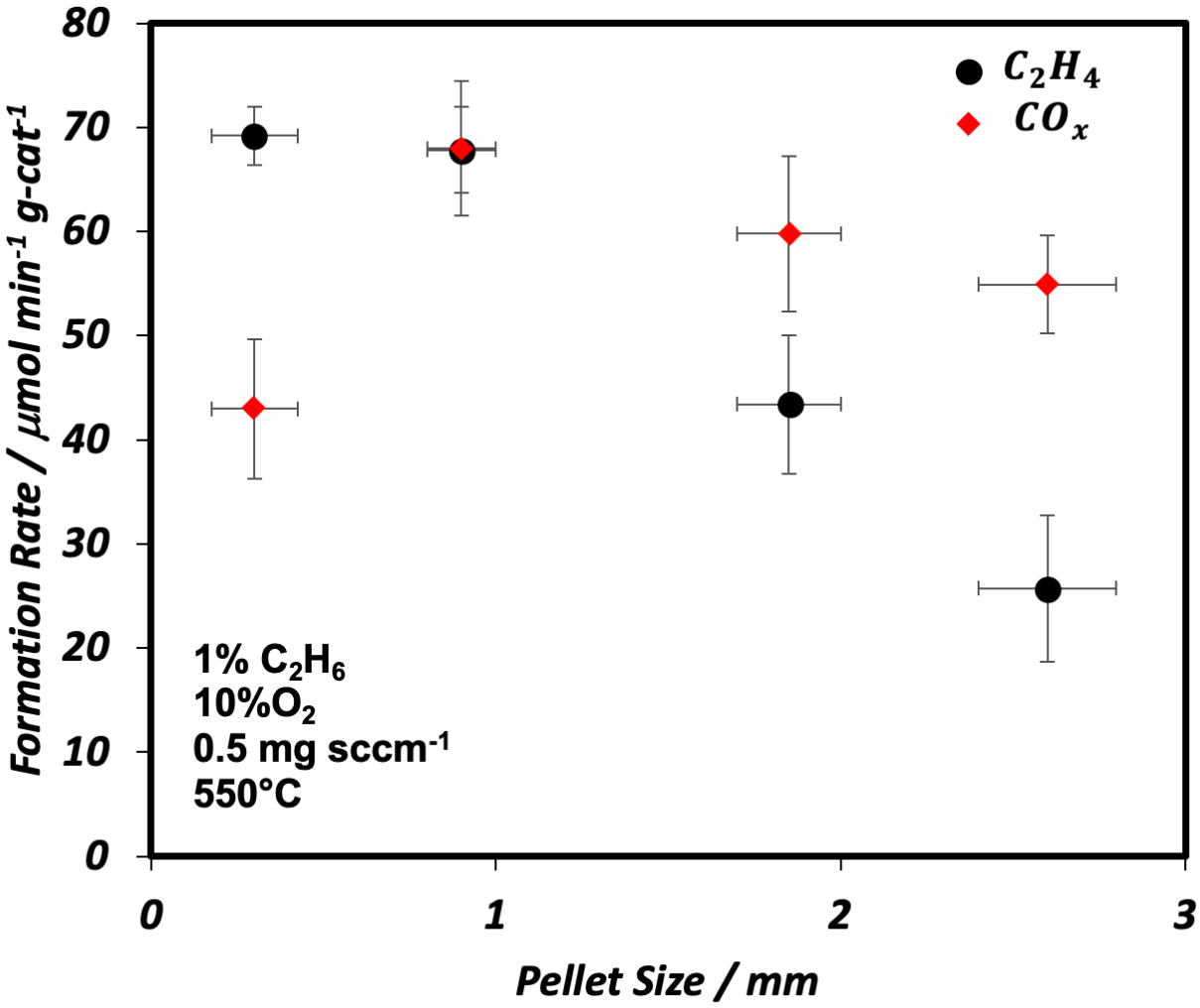

Figure 2: Experimentally measured C_2H_4 and CO_x formation rates at 550°C, 0.5 mg/sccm^{-1}, 1% C_2H_6, 10% O_2 for various catalyst pellet sizes.

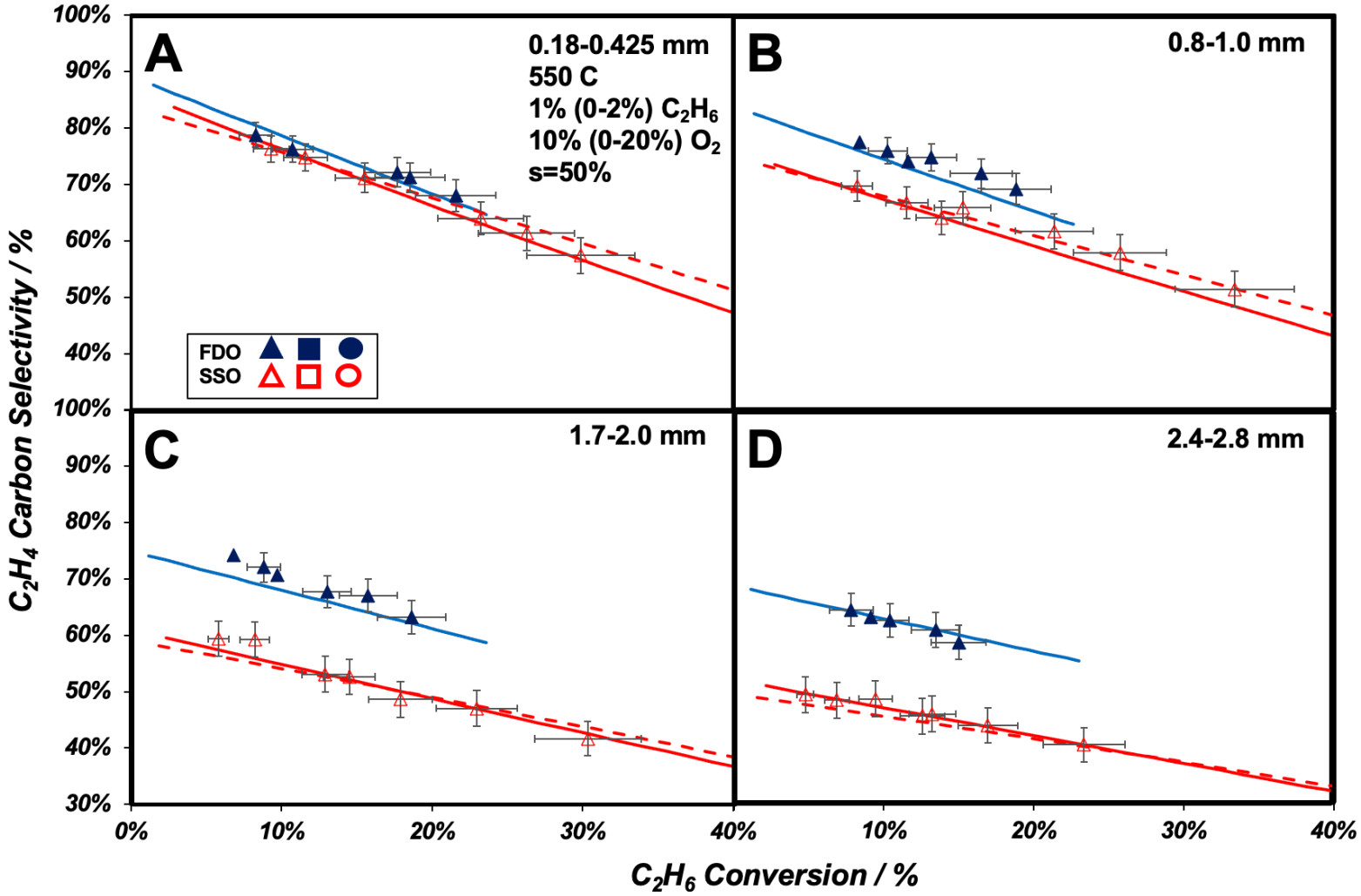

Figure 3: C_2H_4 carbon selectivities as functions of C_2H_6 conversion for 0.3 (A), 0.9 (B), 1.85 (C), and 2.6mm (D) catalyst pellets at 550°C, 1% C_2H_6 and 10% O_2. Reactants were fed out-of-phase with a 50% duty cycle (0-2% C_2H_6 and 20-0% O_2). Solid and dashed lines represent the model and analytical solutions respectively. Experimental data are listed as data points with error bars.

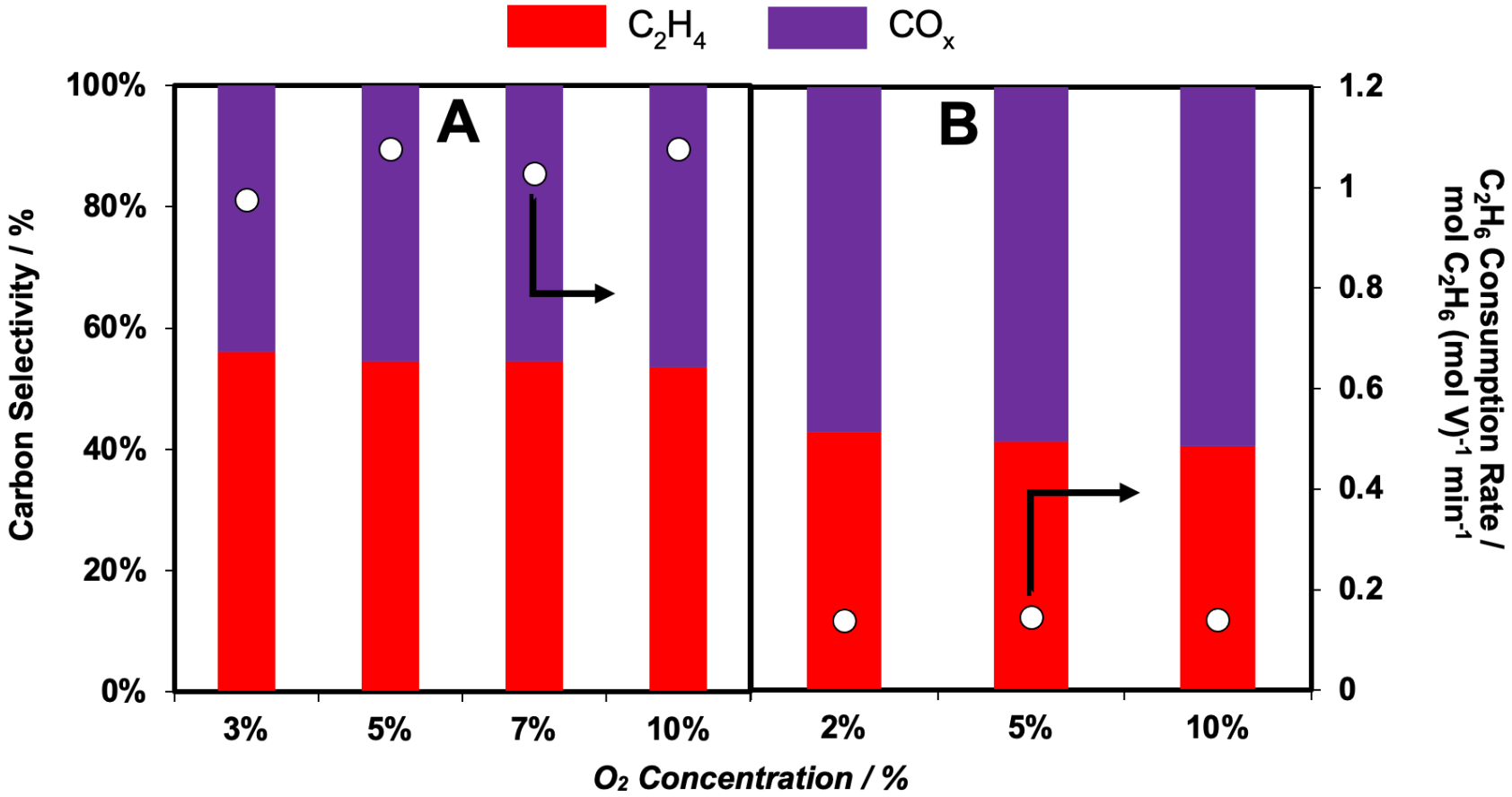

Figure 4: C_2H_4, CO_x carbon selectivities [%] and C_2H_6 consumption rates [mol C_2H_6 (mol V)$^{-1}$ min^{-1}] as functions of O_2 concentration [%] at 3 and 2 mg sccm^{-1}, of 0.18-0.425 (A) and 2.4-2.8mm (B) sized pellets respectively. Experiments were run at 550°C and 1% C_2H_6.

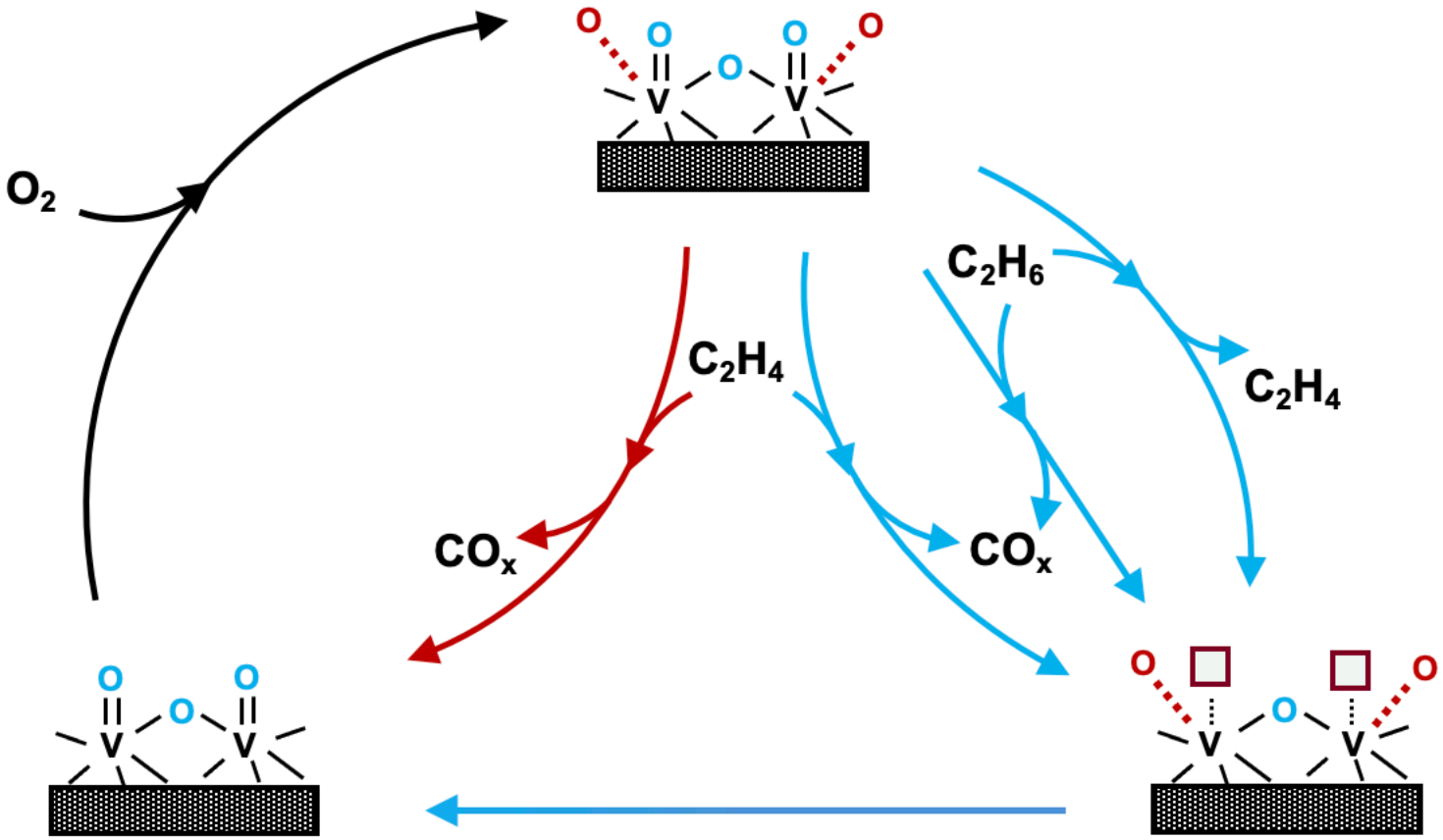

Scheme 2: Reaction pathways used in model with chemisorbed (red) and lattice (blue) oxygens over the VO_x catalyst.

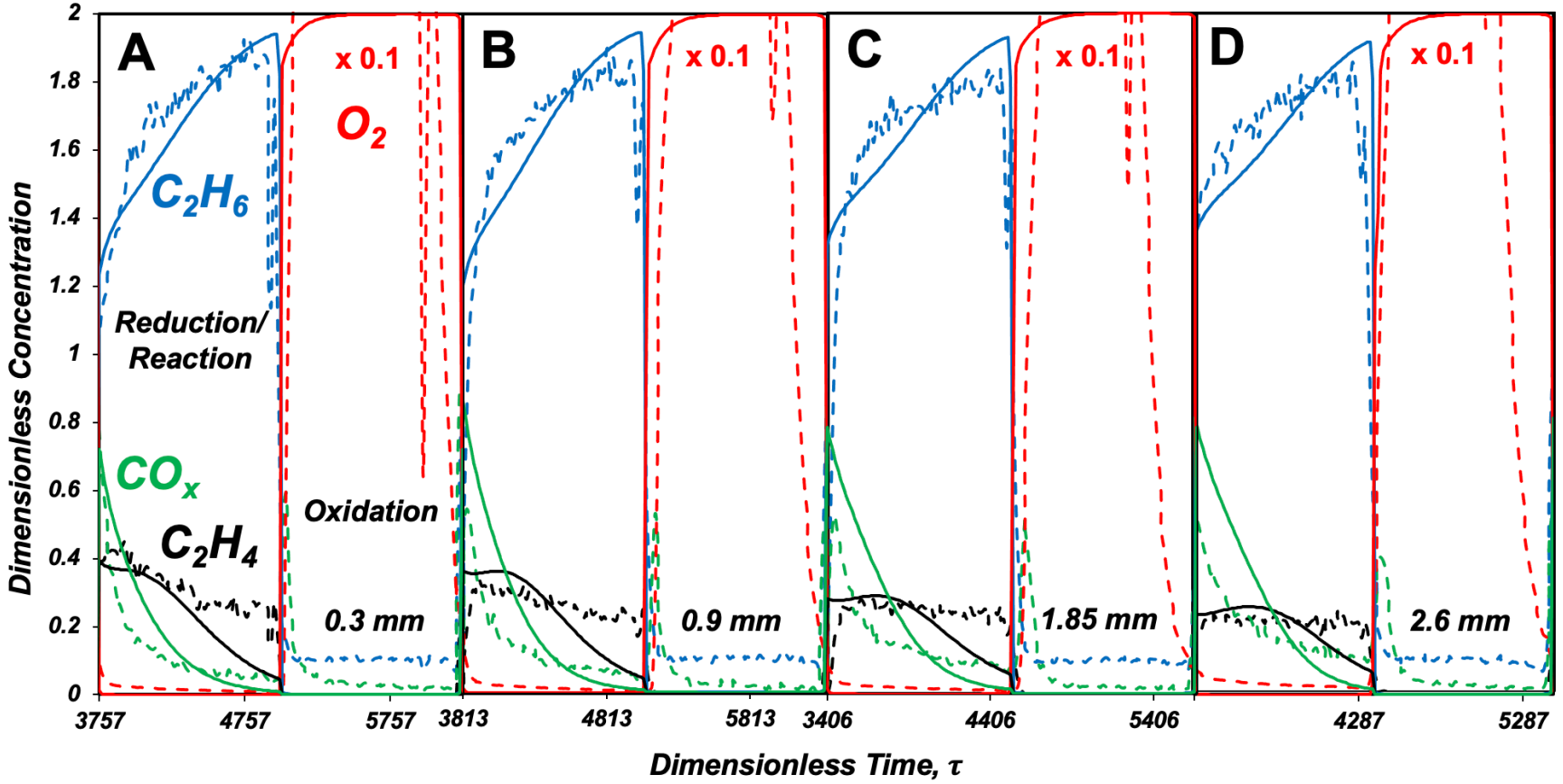

Figure 5: Dimensionless bulk phase concentrations of C_2H_6, O_2, C_2H_4 and CO_x throughout the reactor during FDO for 0.03 (a), 0.09 (b), 1.85 (c) and 2.6 (d) mm pellets measured during experiment and estimated by the model utilizing 1% C_2H_6, 10% O_2 at 550°C. The residence time for each case was adjusted to give the same C_2H_6 conversion (~16%). Note: to prevent mixing between C_2H_6 and O_2 pulses due to axial dispersion at the injection point, the O_2 pulse height and width were increases and decreased respectively such that the total moles of O_2 were held at a constant 10% hence the disagreement between experiment and model at later oxidation times.

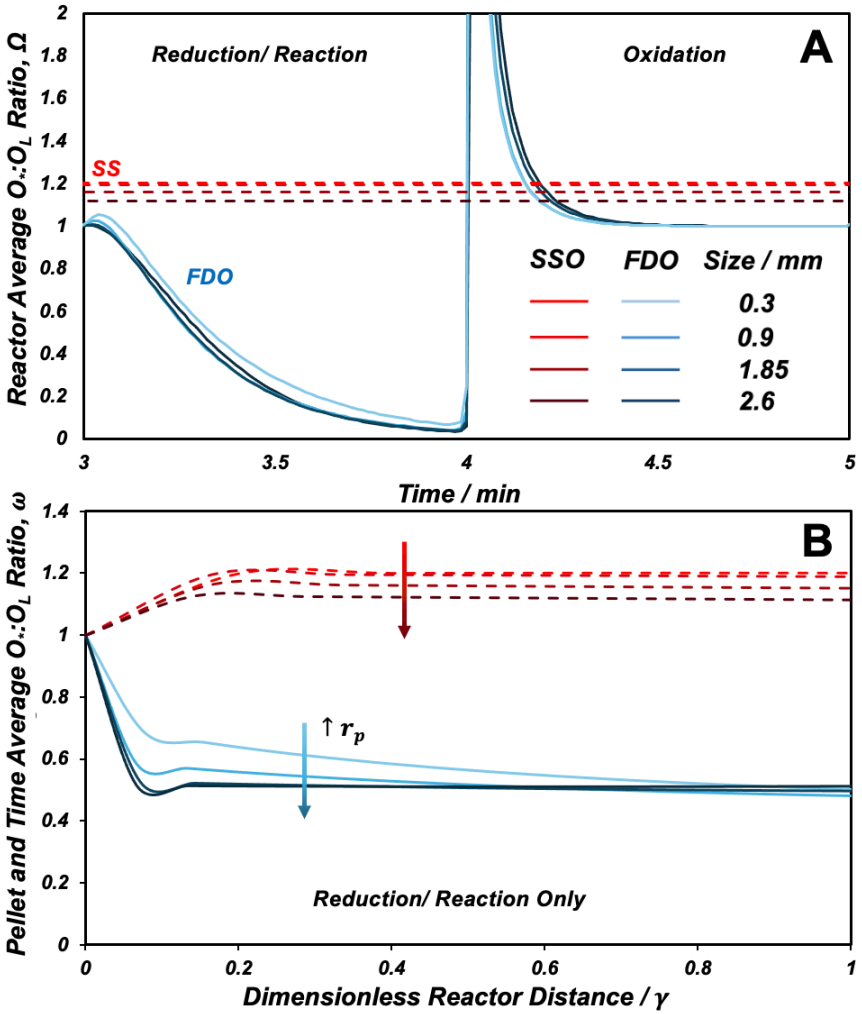

Figure 6: O_*:O_L ratio averaged throughout the reactor (Ω) (A) and averaged over the pellet and reduction time (ω) (B) during FDO and SSO for 0.03, 0.09, 1.85 and 2.6 mm pellets compared at the same SSO and FDO C_2H_6 conversions (~16%) using 1% C_2H_6 and 10% O_2 at 550°C.

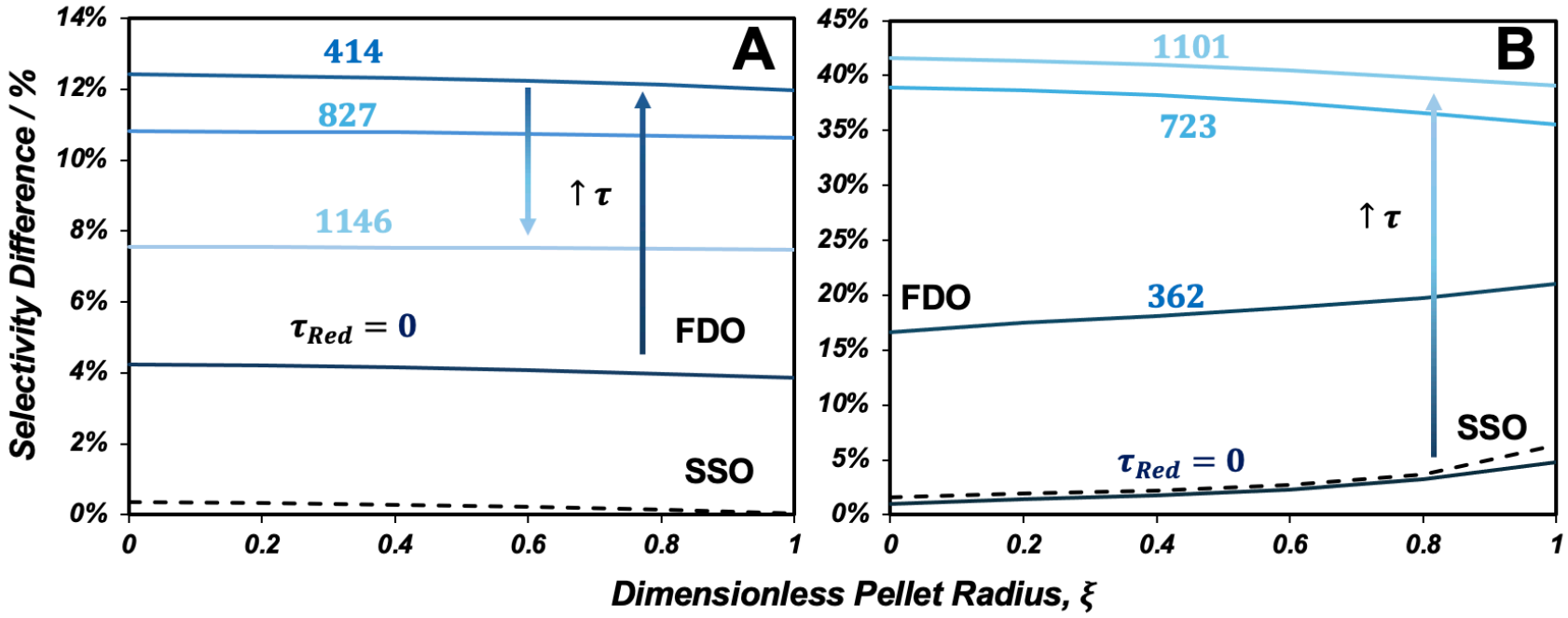

Figure 7: Selectivity difference versus pellet radius located at the center of the reactor at various dimensionless times for 0.3 (A) and 2.6mm (B) catalyst pellets during the reduction half cycle using 1% C_2H_6 and 10% O_2 at 550°C and 16% C_2H_6 conversion.

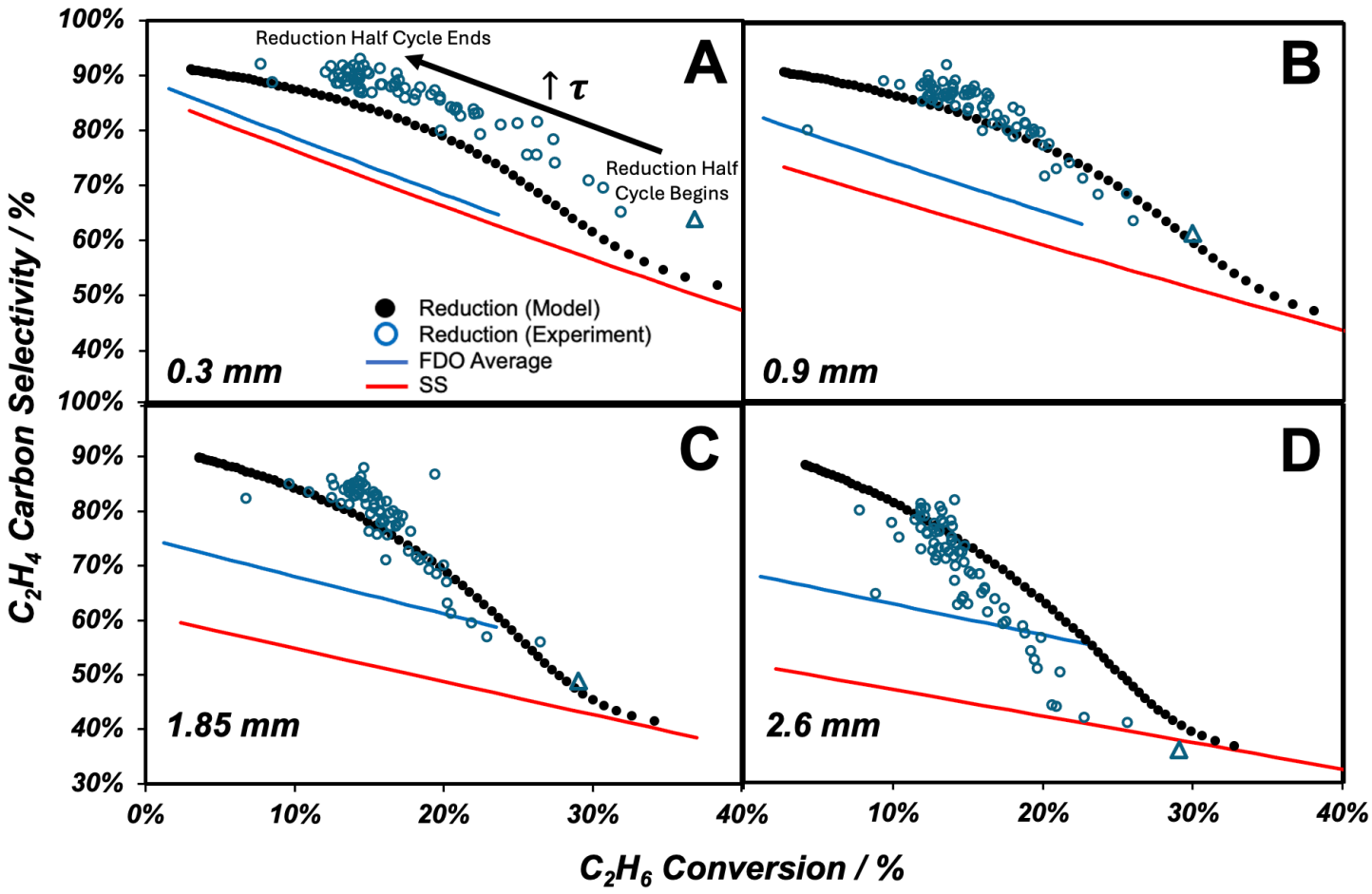

Figure 8: Instantaneous C_2H_4 selectivity versus C_2H_6 conversion in the reactor effluent over time during the reduction half cycle for 0.3 (A), 0.9 (B), 1.85 (C) and 2.6mm (D) catalysts measured during experiment and predicted by the model. SSO and cyclic average FDO values are indicated by solid lines. For example, the average selectivity and conversion of all instantaneous values (data points) are equivalent to ~16% C_2H_6 cycle average conversion.

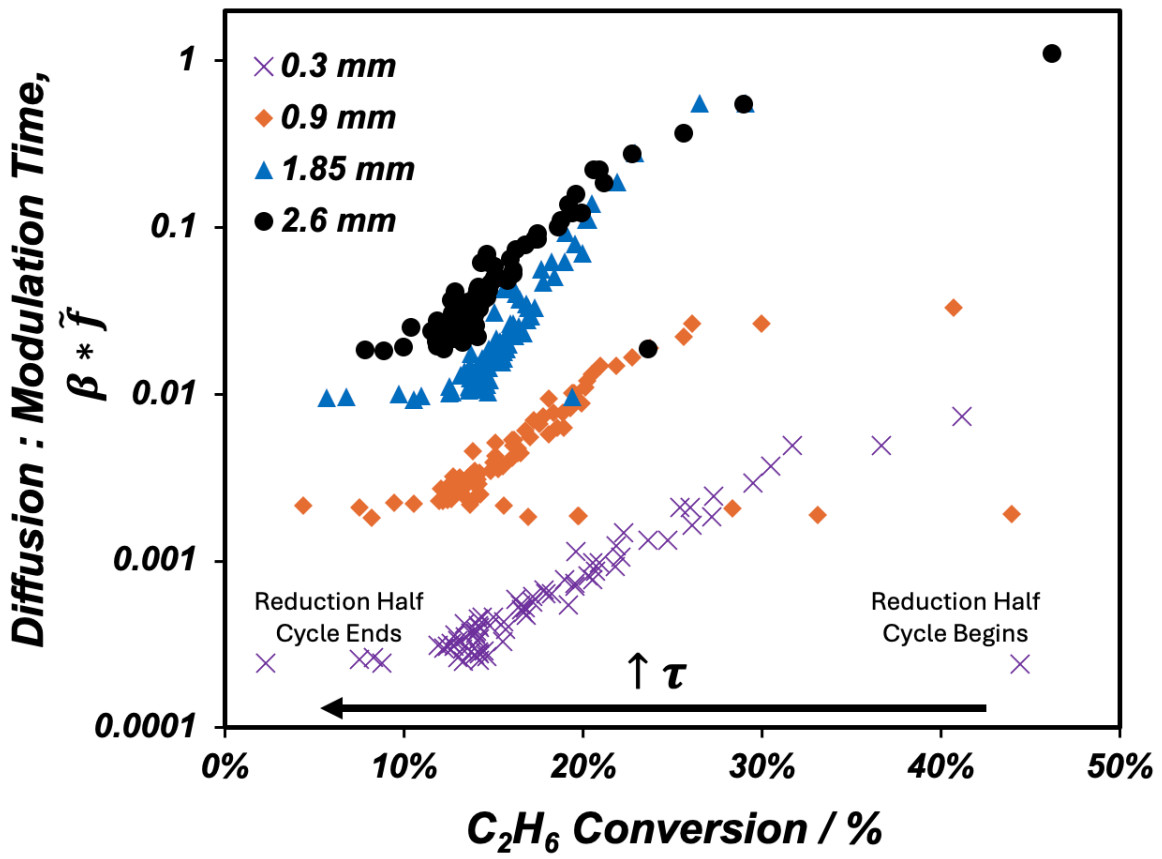

Figure 9: Experimentally estimated ratios of modulation to diffusion time scales versus C_2H_6 conversion in the reactor effluent over time during the reduction half cycle at 16% cycle average C_2H_6 conversion. Note: All data including outliers were used in this plot.

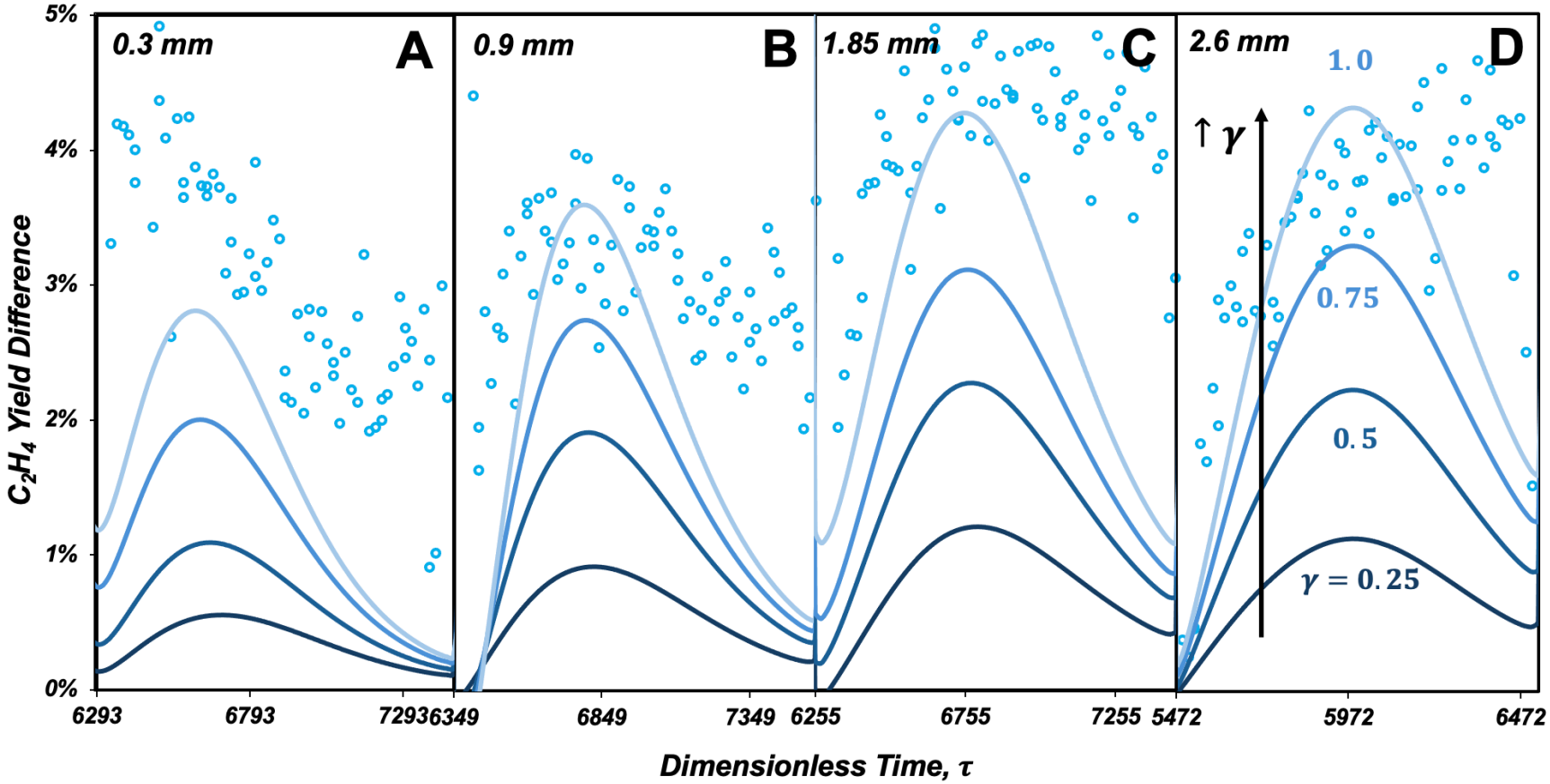

Figure 10: Yield difference as a function of dimensionless time at various points along the reactor (residence times) during the reduction half cycle for 0.3 (A), 0.9 (B), 1.85 (C) and 2.6mm (D) catalyst pellets measured during experiment (circles) and predicted by the model (solid lines). Each reactor was compared at the same effluent C_2H_6 conversion (~16%).